Università degli Studi di Pisa

DIPARTIMENTO DI INGEGNERIA DELL'INFORMAZIONE
Corso di Laurea Magistrale in Ingegneria Robotica e dell'Automazione

Tesi di Laurea Magistrale

Optimization of the Geometry of Communication for Autonomous Missions of Underwater Vehicles

Candidato:
Alessio Micheloni
Matricola 443219

Relatore:
Prof. Andrea Caiti

Controrelatore:
Prof. Lorenzo Pollini

Anno Accademico 2014/2015

"An expert is someone who has made all the possible mistakes which can be made, in a narrow field."
(Niels Bohr, Danish physicist, 1885-1962)

A tutti quelli che mi hanno incoraggiato e sostenuto durante questi sette lunghi anni di carriera universitaria.

Sommario
Il potenziale dei Veicoli Subacquei Autonomi (AUVs) nel monitoraggio, nella sorveglianza e nell'esplorazione dell'ambiente marino è consolidato già da tempo. Uno degli ostacoli più rilevanti nel loro utilizzo risiede tuttavia nelle limitazioni del canale acustico per la comunicazione tra i veicoli. I modelli per la simulazione acustica subacquea hanno un ruolo importante nella predizione di possibili perdite ed errori di trasmissione, in quanto la propagazione del suono sott'acqua può essere misurata o stimata con grande precisione. In questa tesi, dati reali della velocità del suono provenienti da un esperimento (CommsNet 13) sono stati utilizzati nella simulazione delle condizioni ambientali allo scopo di analizzare la comunicazione acustica tra un veicolo USBL sulla superficie del mare e un modem acustico posizionato sul fondale, e poter dimensionare di conseguenza la geometria di trasmissione per future prove.

Abstract
The potential of Autonomous Underwater Vehicles (AUVs) working as a team in sampling, monitoring and surveillance of the marine environment has been realized since quite a long time. One of the most relevant obstacle to their operational implementation resides in the limitations of the acoustic channel for inter-vehicle communications. Underwater acoustic modeling and simulation plays an important role in predicting possible losses and transmission failures between them, and underwater sound propagation can be precisely measured or estimated. In this thesis, sound speed data from a real experiment (CommsNet13) were used to simulate environmental conditions and analyze acoustic communication between an USBL-vehicle on the sea surface and an acoustic modem on the sea bottom, in order achieve an effective geometry of transmission for future trials.

Contents

Introduction

Autonomous Underwater Vehicles (AUVs) possess a great potential in monitoring, surveillance and exploration of the marine environment, especially when working in teams, but their practical implementation is affected by a lot of factors and limitations. Unlike other forms of unmanned vehicles, AUVs can have difficulties communicating underwater. This is mainly due to the action of water distorting transmissions, as well as the multitude of obstacles that the robot must maintain an awareness of. The robot's ability to communicate in real-time is extremely hindered during submerged operations. Also, the problem of navigation and self-localization is particularly challenging in an underwater context due to the tight environmental constraints, such as the absence of an absolute positioning system, i.e. GPS, and the small communication bandwidth of the acoustic channel.

Underwater communication is difficult due to factors like multipath propagation, time variations of the channel, small available bandwidth and strong signal attenuation, especially over long ranges. In underwater communication there are low data rates compared to terrestrial communication, since underwater communication uses acoustic waves instead of electromagnetic waves, which are strongly attenuated and therefore impossible to use. One of the most important parameter in this context is the sound speed, since it is the main influence on acoustic ray paths (together with top and bottom reflections).

In this thesis, real sound speed data recorded during the experiment CommsNet13 were used in a numerical simulator (BELLHOP) in order to characterize the underwater environment and to predict how wave energy propagates in the channel. This served as the basis for the consequent analysis of acoustic communication between a vehicle on the surface and an acoustic modem fixed on the sea bottom, which can encounter possible losses and transmission failures.

The thesis is organized as follows. Chapter 1 is a brief collection and description of the state of art in AUV navigation and localization. In particular, the main technologies of acoustic localization are presented and explained.

Chapter 2 describes the CommsNet13 experiment, which proposed a mixed USBL-LBL approach for the localization of the autonomous vehicle Typhoon. The sound speed data collected during these trials formed the basis for the development of this thesis.

Chapter 3 introduces the reader to the basic concepts of underwater acoustics. The main oceanographic quantities and the acoustical properties of the ocean environment are described, together with the typical propagation paths of sound waves in underwater environments. The chapter is concluded with the mathematical derivation of the wave equation both in the time and frequency domains

(the Helmholtz equation), which forms the basis for numerical models, and a brief discussion on the principle of acoustic reciprocity.

Chapter 4 briefly describes the computer models available for underwater acoustic simulation, with a focus on the general theory of one of them, ray tracing, for two reasons: it is the most intuitive and largely used in real applications; and it was the one we used to generate and analyze all the results presented in this work. A quick user guide which explains how to set a simulation with the numerical simulator BELLHOP is included in Appendix D.

In Chapter 5, all the results obtained from the simulations of the acoustic environment and experimental conditions of CommsNet13 trials are presented and discussed. These are: ray plots, in order to see how energy propagates through the acoustic channel; transmission loss, to quantify signals attenuation; and source-receiver arrivals, which constitute the impulse response of the channel.

The latter are the main focus of Chapter 6, which includes an extensive analysis of how signals are transmitted from source to receiver. To test the correct reception of the source signal, correlation analysis is used, and the receiver could try to estimate the real source signal from the received one in order to get rid of multipath interference. All the mathematical tools used for this scope (received signal calculation, impulse response and source signal estimations) are described in Appendices A to C.

Finally, the thesis is concluded with a discussion of the work presented and the results achieved by the proposed solutions.

Chapter 1

AUV Navigation and Localization

The development of Autonomous Underwater Vehicles (AUVs) began in the 1970s. Since then, advancements in the efficiency, size, and memory capacity of computers have enhanced their potential. AUVs designs include torpedo-like, gliders, and hovering, and their sizes range from human portable to hundreds of tons.

AUVs are now being used for a wide variety of tasks, including oceanographic surveys, demining, and bathymetric data collection in marine and riverine environments. Accurate localization and navigation is essential to ensure the accuracy of the gathered data for these applications.

A distinction should be made between navigation and localization. Navigational accuracy is the precision with which the AUV guides itself from one point to another. Localization accuracy is the error in how well the AUV localizes itself within a map.

AUV navigation and localization is a challenging problem due primarily to the rapid attenuation of high frequency signals and the unstructured nature of the undersea environment. Above water, most autonomous systems rely on radio or spread-spectrum communications and global positioning. However, underwater, such signals propagate only short distances due to the rapid attenuation and acoustic-based sensors and communication perform better.

AUV navigation and localization techniques can be categorized according to figure 1.1. In general, these techniques fall into one of three main categories:

- *Inertial/dead reckoning*: Inertial navigation uses accelerometers and gyroscopes for increased accuracy to propagate the current state. It is described in Section 1.1.

- *Acoustic transponders and modems*: Techniques in this category are based on measuring the *Time of Flight* (TOF) of signals from acoustic beacons or modems to perform navigation. They are described in Section 1.2.

- *Geophysical*: Techniques that use external environmental information as references for navigation. This must be done with sensors and processing that are capable of detecting, identifying, and classifying some environmental features (Section 1.3).

The type of navigation system used is highly dependent on the type of operation or mission and in many cases different systems can be combined to yield increased

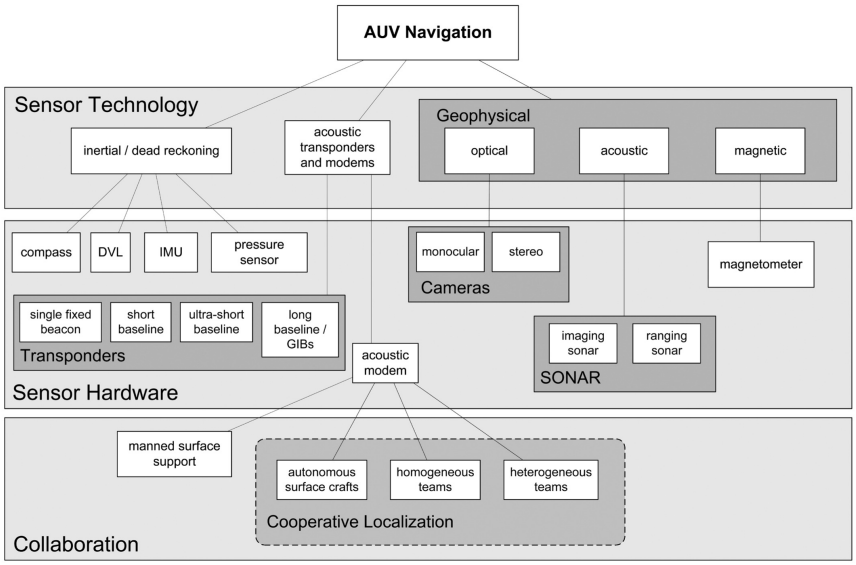

Figure 1.1: Outline of underwater navigation classifications (adapted from [1]).

performance. The most important factors are usually the size of the region of interest and the desired localization accuracy.

The contents of this chapter were developed using review papers [1–3] as the main reference materials.

1.1 Inertial Navigation

When the AUV positions itself autonomously, with no acoustic positioning support from a ship or acoustic transponders, we say that it *dead reckons*. With dead reckoning (DR), the AUV advances its position based upon knowledge of its orientation and velocity or acceleration vector. Traditional DR is not considered a primary means of navigation but modern navigation systems, which depend upon DR, are widely used in AUVs. The disadvantage of DR is that errors are cumulative. Consequently, the error in the AUV position grows unbounded with distance traveled.

One simple method of DR pose estimation, for example, if heading is available from a compass and velocity is available from a Doppler Velocity Log (DVL), is achieved by using the following 2D kinematic equations:

$$\begin{aligned} \dot{x} &= v\cos\psi + w\sin\psi, \\ \dot{y} &= v\sin\psi + w\cos\psi, \\ \dot{\psi} &= 0. \end{aligned} \tag{1.1}$$

where (x, y, ψ) is the state vector (position and heading) in the standard North-East-Down (NED) coordinate system, and (v, w) are the body frame and starboard velocities. In this model, it is assumed that roll and pitch are zero and that depth is measured accurately with a depth sensor.

An Inertial Navigation System (INS) aims to improve upon the DR pose estimation by integrating measurements from accelerometers and gyroscopes. Inertial

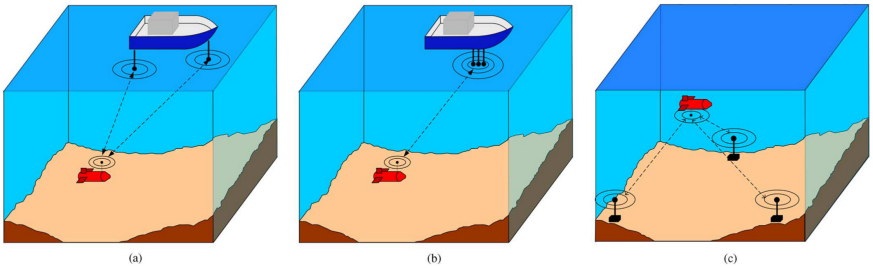

Figure 1.2: Time of flight acoustic localization (adapted from [1]).

proprioceptive sensors are able to provide measurements at a much higher frequency than acoustic sensors that are based on the TOF of acoustic signals (see Section 1.2). As a result, these sensors can reduce the growth rate of pose estimation error, although it will still grow without bound.

One problem with inertial sensors is that they drift over time. One common approach, for example, is to maintain the drift as part of the state space. Slower rate sensors are then effectively used to calibrate the inertial sensors. The performance of an INS is largely determined by the quality of its inertial measurement units. In general, the more expensive is the unit, the better is the performance. However, the type of state estimation also has an effect. The most common filtering scheme is the EKF (Extended Kalman Filter), but others have been used to account for the linearization and Gaussian assumption shortcomings of the EKF (Unscented Kalman Filter, Particle Filters,...). Improvements can also be made to INS navigation by modifying state equations (1.1) to provide a more accurate model of the vehicle dynamics.

Inertial sensors are the basis for an accurate navigation scheme, and have been combined with other techniques described in Sections 1.2 and 1.3. In certain applications, navigation by inertial sensors is the only option. For example, at extreme depths where it is impractical to surface for Global Positioning System (GPS), an INS is used predominantly.

1.2 Acoustic Transponders

In acoustic navigation techniques, localization is achieved by measuring ranges from the TOF of acoustic signals. Common methods include the following:

- *Ultrashort Baseline (USBL)*: The transducers on the transceiver are closely spaced with the approximated baseline on the order of less than 10 cm. Relative ranges are calculated based on the TOF and the bearing is calculated based on the difference of the phase of the signal arriving at the transceivers. See figure 1.2(b).

- *Short Baseline (SBL)*: Baseline are placed at opposite ends of a ship's hull. The baseline is based on the size of the support ship. See figure 1.2(a).

- *Long baseline (LBL)*: Beacons are placed on the seabed over a wide mission area. Localization is then based on triangulation of acoustic signals. See

figure 1.2(c).

- *Acoustic Modems*: The recent advances with acoustic modems have allowed for new techniques to be developed. Beacons no longer have to be stationary, and full AUV autonomy can be achieved with support from autonomous surface vehicles, equipped with acoustic modems, or by communicating and ranging in underwater teams.

Due to the latency of acoustic updates, state estimators are implemented where the DR proprioceptive sensors provide the predictions and the acoustic measurements provide the updates. This is called *Integrated INS*, and is a widely used navigation technique.

1.2.1 Baseline Methods

USBL navigation allows an AUV to localize itself relative to a surface ship. Relative range and bearing are determined by TOF and phase differencing across an array of transceivers, respectively. A typical setup would be to have a ship supporting an AUV. In SBL, transceivers are placed at either end of the ship hull and triangulation is used. The major limitation of USBL is the range, and of SBL is that the positional accuracy is dependent on the size of the baseline, i.e. the length of the ship.

In LBL navigation, localization is achieved by triangulating acoustically determined ranges from widely spaced fixed beacons. In most cases, the beacons are globally referenced before the start of the mission by a surface ship, a helicopter, or even other AUVs. In normal operation, an AUV would send out an interrogation signal, and the beacons would reply in a predefined sequence. The Two-Way Travel Time (TWTT) of the acoustic signals is used to determine the ranges. One of the limitations of LBL is the cost and time associated with setting up the network. Other major drawbacks of LBL are the finite range imposed by the range of the beacons and the reliance on precise knowledge of the local sound-speed profile of the water column based on temperature, salinity, conductivity, and other factors. However, LBL systems often do overcome these shortcomings to be one of the most robust, reliable, and accurate localization techniques available. For that reason, it is often used in high-risk situations such as under-ice surveys.

1.2.2 Acoustic Modems

Advances in the field of acoustic communications have had a major effect on underwater navigation capabilities. The acoustic modem allows simultaneous communication of small packets and ranging based on TOF. If the position of the transmitter is included in the communication information, then the receiver can bound its position to a sphere centered on the transmitter. This capability removes the need for beacons to be fixed or localized prior to the mission. In addition, it allows for inter-AUV communication, which means that teams of AUVs can cooperatively localize.

Popular acoustic modems are manufactured by the Woods Hole Oceanographic Institute (Woods Hole, MA, USA) [4], Teledyne Benthos (Thousand Oaks, CA, USA) [5], and EvoLogics (Berlin, Germany) [6], among others.

The ability of a modem at the surface to transmit its location to the survey vehicles provides two important benefits over past navigation methods: 1) it removes the necessity to georeference the beacons before starting the mission; and 2) it allows the beacons to move during the missions. The first advantage saves time and money, and the second allows the mission range to be extended as necessary without redeploying the sensor network. Many methods have been recently published that exploits one or both of these benefits.

In some cases, certain AUVs are outfitted with more expensive sensors and/or make frequent trips to surface for GPS position fixes. These vehicles support the other survey vehicles and have been referred to as Communication/Navigation Aids (CNAs) in the framework of *Cooperative Navigation* (CN). Position error will grow slower if the AUVs are able to communicate their relative positions and ranges. If the CNAs (or any vehicle, for the case of homogeneous teams) surfaces for a position fix, then the information can be shared with the rest of the team to bound the position error.

1.3 Geophysical Navigation

Geophysical navigation refers to any method that utilizes external environmental features for localization. Almost all methods in this category that achieve the bounded position error use some form of SLAM (*Simultaneous Localization and Mapping*). Categories include the following:

- *Optical*: Use of a monocular or stereo camera to capture images of the seabed and then match these images to navigate.
- *Sonar*: Used to acoustically detect then identify and classify features in the environment that could be used as navigation landmarks.

Limitations for optical systems in underwater environments include the reduced range of cameras, susceptibility to scattering, and inadequacy of lighting. As a result, visible wavelength cameras are more commonly installed on hovering AUVs because they can get close to object of interest. In addition, visual odometry (the process of determining the vehicle pose by analyzing subsequent camera images) and feature extraction relies on the existence of features. Therefore, optical underwater navigation methods are particularly well suited to small-scale mapping of feature-rich environments. Examples include ship hulls or shipwreck inspections.

Sonar imaging of the ocean has become well established by decades, therefore it is a fairly robust technology. Several types of sonars are used for seabed and structure mapping, and they are designed to operate at specific frequencies depending on the range and resolution required. In all cases, the performance of the SLAM algorithm is dependent on the number and quality of the features present in the environment. The image post-processing to detected the features for data association (when required) can be done directly onboard AUVs.

Chapter 2

The CommsNet13 Experiment

Underwater navigation is still a challenging task for AUVs, requiring a trade-off between performance and cost. Inertial Navigation Systems (INS) of marine and navigation grade may have an horizontal drift as limited as less than 2000 m per day, but at costs that can reach and overcome 1 Million € (unaided INS are considered here, i.e. inertial systems without support from additional sensors).

In the case of AUVs working in shallow water for environmental exploration and monitoring, possibly in team, there is an absolute need of keeping the cost of any individual vehicle within reasonable bounds. As a consequence, these systems require a navigation procedure able to compensate the error drift of the on-board INS, in any.

In the framework of the THESAURUS project (Italian acronym for "TecnicHe per l'Esplorazione Sottomarina Archeologica mediante l'Utilizzo di Robot aUtonomi in Sciami") a class of AUVs (called Typhoon) able to cooperate in swarms to perform navigation, exploration and surveillance of underwater archaeological sites has been developed.

During the CommsNet13 experiment, which took place in September 2013 in the La Spezia Gulf, North Tyrrhenian Sea, one of these vehicles was used to test a mixed USBL/LBL system for navigating an AUV within a pre-specified area. The AUV was equipped with a USBL sensor, capable also to communicate as an acoustic modem; the LBL anchors were acoustic modems deployed at the seabed in a-priori unknown locations. The AUV was also equipped with an Inertial Measurement Unit (IMU), and with a Global Positioning System (GPS) receiver antenna.

Conceptually, the proposed localization procedure is as follows:

- *Initialization Phase*: the AUV, navigating at the sea surface (knowledge of absolute position in a standard NED frame is available thanks to GPS receiver), interrogates repeatedly the moored modems, not necessarily from the same position. The measured relative positions are the transformed into absolute positions by exploiting the GPS information on the absolute position of the USBL modem (i.e. the one mounted on the vehicle). The set of measured absolute positions from each moored modem is averaged, in order to obtain a final estimate of each moored modem absolute position.

- *Navigation Phase*: the AUV navigates with the GPS turned off, pinging the moored modems and measuring the relative position of the moored modems

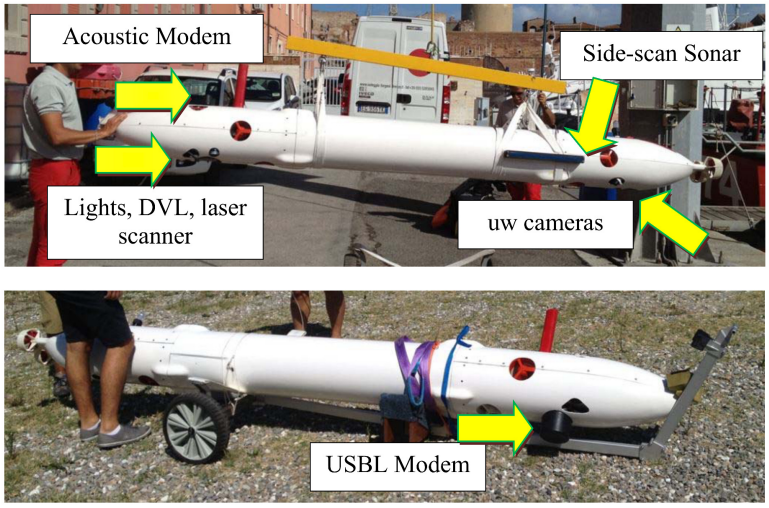

Figure 2.1: Two Typhoon vehicles, the top one with standard acoustic modem and payloads for underwater search, the bottom one with USBL modem.

with respect to the on-board USBL modem; taking into account the knowledge of the moored modem absolute position, the USBL modem relative position is transformed into an absolute position. This absolute position estimate is fed to the navigation filter, fusing together IMU measurement and acoustic position estimates in order to reduce the drift of inertial navigation.

Section 2.1 describes the Typhoon class of vehicles, its primary design requirements and the on-board equipment and payload. Section 2.2 illustrates the acoustic localization procedure previously introduced, and the results obtained are presented and briefly discussed. Finally, Section 2.3 introduces the sound speed data recorded during the experiment and explains how these form the basis for the following developments.

The contents of this chapter were developed using papers [7–12] as the main reference materials.

2.1 The Typhoon Class Vehicles

The primary design requirements for the Typhoon vehicles are: maximum operating depth of 250 meters; autonomy ranging from 8 to 10 hours; maximum speed of 5-6 knots[1]; and low cost.

Typhoon class vehicles can be divided into three different categories:

- *Vision Explorer*: A vehicle equipped with cameras, laser and structured lights for an accurate visual inspection and surveillance of archaeological sites. Visual inspection involves a short range distance (few meters) between the vehicle and the target site, and the capability of performing precise maneuvering and hovering.

[1]Remember that 1 knot = 0.5 m/s.

- *Acoustic Explorer*: Preliminary exploration of extended area to recognize potentially interesting sites involves the use of acoustic instruments, such as side-scan sonar. This kind of vehicle can perform long range, extended missions. Consequently, navigation sensors able to compensate the drift of the inertial sensors, such as DVL, have to be installed on board.

- *Team Coordinator*: A vehicle with extended localization and navigation capabilities is used to coordinate the team. This vehicle periodically returns to surface providing the GPS positioning and, more generally, detailed navigation information that can be shared with other vehicles of the team (this is the approach described in Section 1.2.2).

In accordance with the project requirements, a hybrid design, able to satisfy different mission profiles, has been preferred, to reduce the engineering and production costs and to assure vehicles interchangeability. Each vehicle of the team can be customized for different mission profiles (see figure 2.1).

2.1.1 The Typhoon Hardware

Typhoon vehicles are middle-sized class AUVs, whose features are comparable with other existing vehicles. The vehicle sizes are: length of about 3.6 m; external diameter of about 350 mm; weight of 130-180 kg according to the carried payload.

Since every vehicle can be customized to manage different payloads and mission profiles, the system was designed by dividing the on board subsystems in two main categories:

- *Vital Systems*: all the navigation, communication and safety related components and functions of the vehicle are controlled by an industrial PC-104, called Vital PC, whose functionality is continuously monitored by a watchdog system. Most of the code implemented on the Vital PC is quite invariant with respect to the mission profiles and payloads, assuring a high reliability of the system.

- *Customizable Payloads*: all the additional sensors and functions related to variable payloads are managed by one or more Data PC. In particular, the Data PC also manages the storage on mass memories (conventional hard disks or solid state memories) and the data coming from the connected sensors. This way, all the processes introduced by additional payloads are implemented on a platform which is also physically separated from the vital one; from an electrical point of view the two parts are protected independently through fuses and relays.

For completeness here is reported a list of the on board sensors and payloads:

- Inertial Measurement Unit (IMU) Xsens MTi: device made up of a 3D gyroscope, 3D accelerometer and 3D magnetometer furnishing dynamic data at a maximum working frequency of 100 Hz. The device measures the orientation of the vehicle in a 3D space in an accurate way thanks to an estimate inner owner algorithm.

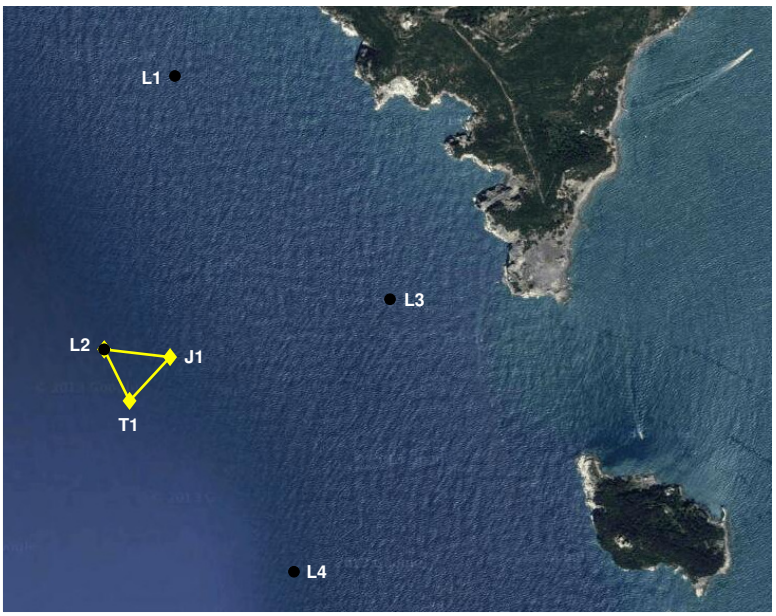

Figure 2.2: Mission area for Sept. 22$^{\text{th}}$ experimental run (adapted from [7]).

- Doppler Velocity Log (DVL) Teledyne Explorer: sensor measuring the linear speed of the vehicle, with respect to the seabed or with respect to the water column beneath the vehicle. Moreover, if it detects the seabed it is also able to measure the distance from it (like an altimeter).
- Acoustic modems (single modem or USBL-enhanced) by EvoLogics: for underwater communication and localization.
- Echo Sounder Imagenex 852: single beam sensor, mounted in the bow of the vehicle and pointing forward. It can measure the distance from the first obstacle(s) placed in front of the vehicle.
- STS DTM depth sensor: digital pressure sensor used to measure the vehicle depth.
- PA500 echo sounder, pointing downward, to measure the vehicle elevation from the seabed.
- Tritech Side Scan Sonar (675 kHz) for acoustic survey of the seabed.

The reader should refer to papers [8, 9] for a more detailed description of Typhoon's hardware, propulsion system and communication network protocol.

2.2 Acoustic Localization

2.2.1 Experimental Configuration

The CommsNet13 cruise was organized and scientifically led by the NATO Science & Technology Organization Center for Maritime Research and Experimentation

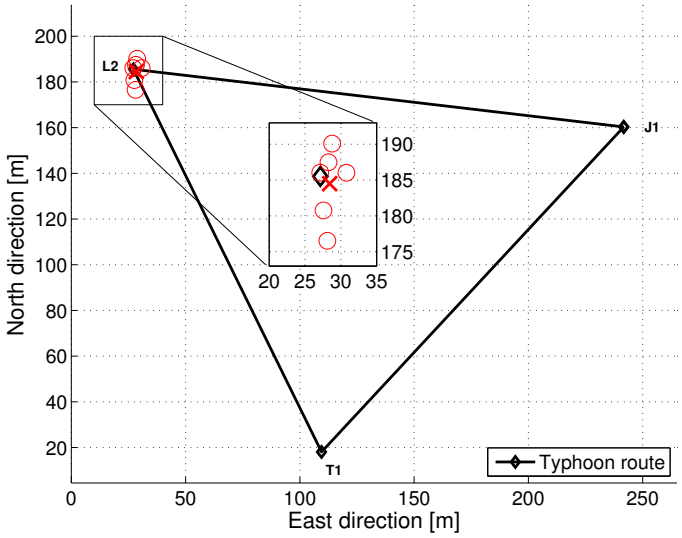

Figure 2.3: Initialization phase for estimating the position of the LOON modem L2 (adapted from [7]).

(CMRE), and had the broad objective of testing and comparing methodologies for underwater communication, localization and networking. Several research institutions were invited to participate in the testing, that took place from Sept. 9th to 22th 2013 in the Gulf of La Spezia, North Tyrrhenian Sea, and was operated from the R/V Alliance.

The ISME groups of the Universities of Pisa and Florence jointly participated to the cruise bringing two Typhoon AUVs, but only the vehicle with USBL-modem capabilities has been used in the test. The AUV has been operated from surface, to have the availability of the GPS signal to be used as ground truth, and underwater, at a depth of almost 5-6 m.

Figure 2.2 shows the CMRE underwater network installation, named LOON, for the 22th experimental run near Palmaria Island. It consisted of four EvoLogics acoustic modems L1, L2, L3 and L4 deployed close to the sea bottom. The reference path for the mission consisted in the triangle (approximately 150 m per side) defined by waypoints J1, L2 (position of the second one of the four LOON modems) and T1. While navigating, the AUV was obtaining the relative position of the moored modems through its on-board USBL modem. The modems were operated at the lowest power level allowed by the instrumentation.

More details on the experimental procedure can be found in [7].

2.2.2 Initialization Phase

Within this phase the GPS information (i.e. the AUV position in the NED absolute reference frame) is used to convert the relative position of the moored modems with respect to the AUV body frame into the moored modems absolute position in the NED frame. Several absolute position estimates are thus obtained for each moored modem and, after outlier inspection and removal, the average of the measured

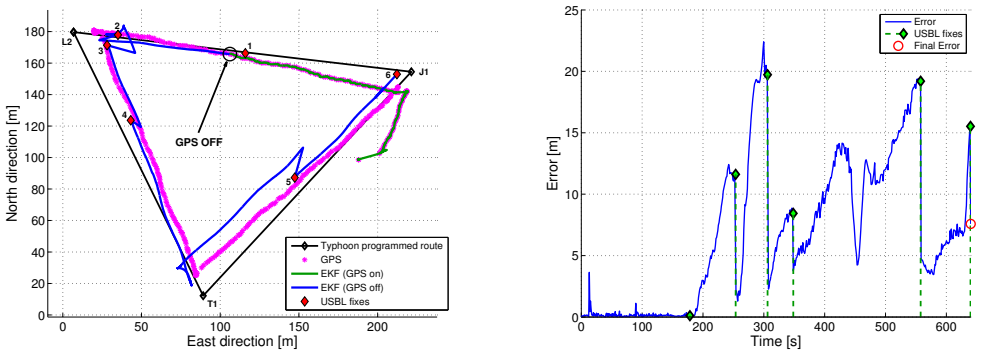

(a) (b)

Figure 2.4: Estimated path and navigation error for Sept. 22$^{\text{th}}$ run (adapted from [7]).

positions was taken as absolute position for each moored modem, to be used as such in the navigation phase.

Figure 2.3 shows the results for the localization of the L2 modem of the LOON network. The actual position of the modem is represented by the black diamond (see enlargement), while red circles are the position measurements obtained with USBL localization; these were averaged (after outliers removal) to obtain the position estimate, represented by the red cross. This figure highlights the precision and accuracy in acoustic measurements for this phase of the experiment.

2.2.3 Navigation Phase

Within the navigation phase, the position was estimated using: IMU measurements at 10 Hz rate; acoustic absolute position measurements, obtained from the USBL-modem relative to moored modems, and accounting for the absolute moored modems position. Acoustic positioning data comes at irregularly spaced intervals; moreover, since the position interrogation of the modem was embedded in a networked communication protocol, including round-robin interrogation of all the possible modems, the delays due to such protocol were non negligible. The combined effect of network overburden and communication loss due to acoustic channel effects resulted in intervals between successive acoustic measurements of the order of tens of seconds, irregularly spaced in time throughout the experiment.

The available measurements were fused together through an Extended Kalman Filter (EKF); the filter weights were set in such a way to give more importance to the acoustic measurements with respect to IMU measurements. For a detailed discussion on the filtering algorithm, see [11, 12]. Note that the AUV had no direct velocity measurements (for instance, no DVL were used.)

2.2.4 Results and Discussion

The estimated path for Sept. 22$^{\text{th}}$ run of the experiment is reported in figure 2.4(a), together with the GPS path, which is taken as ground truth comparison. The

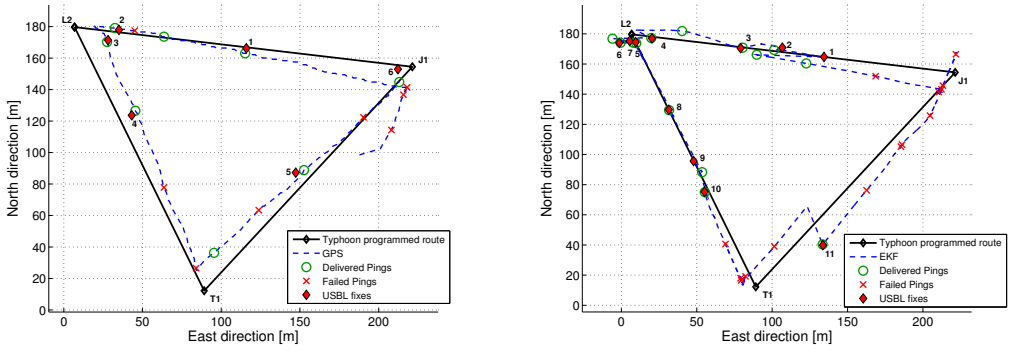

(a) (b)

Figure 2.5: Acoustic performance of the LOON installation for two Sept. 22$^{\text{th}}$ runs (adapted from [7]).

red diamonds in the figure indicates the acoustic position measurements. In figure 2.4(b) we also report the estimation error, computed as the distance (norm) in meters between the filter estimated position and the GPS position as a function of time. The diamonds represent the instant in time in which an acoustic position measurement is received by the filter.

From both figures it can be noted the expected drift in position estimate in the absence of acoustic measurements data (when navigation relies on IMU dead reckoning only), and how the acoustic position fixes are effective in decreasing the navigation error. As an additional consideration, it is notable how the interval in time between two successive measurements can indeed be of minute scale. As already commented, there are two significant sources of delay in this setup: one is the communication structure, the other is the variability of the channel with consequent loss of position messaging.

Figure 2.5 shows the spatial distribution of the modem interrogations: in particular, the green circles and the red crosses indicate the position of the vehicle at the time instant of an acoustic ping, respectively successful or not. A new USBL measurement, indicated by the red diamond, occurs as a result of a delivered ping; however, it is evident that not all the successful interrogations provide a positioning information. As can be expected, the acoustic communication is strongly dependent on the vehicle position at the moment of the interrogation. This correlation between transmission successes/failures and the position of the vehicle suggested us to collect environmental data and further investigate how the acoustic channel (whose properties change with position) influences signal propagation.

2.3 Recorded Sound Speed Data

Figure 2.6 depicts the underwater sound speed data recorded using a CTD sensor in the Gulf of La Spezia on the Sept. 14$^{\text{th}}$ experimental run, both for morning and afternoon periods of the day. Sound speed is the most important parameter in ocean acoustics (as we will see extensively in Chapter 3), and CTD sensors are

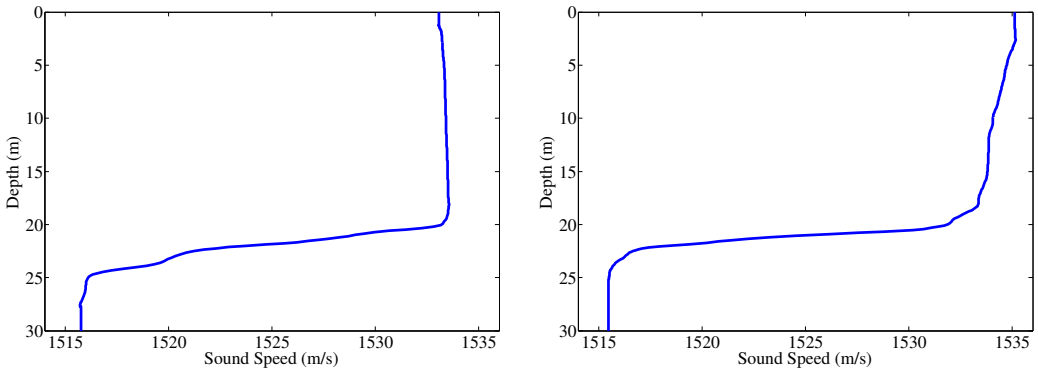

(a) (b)

Figure 2.6: Sound speed profiles recorded during CommsNet13 sea trials on Sept. 14^{th} run.

oceanographic instruments used to determine the conductivity, temperature and depth of the ocean[2]. As we can see, morning and afternoon profiles are very similar. They both possess a strong negative gradient near the sea bottom, and the only difference is in the upper part (constant for morning, linear for afternoon), that is very sensitive to atmospheric and climatic factors.

These data were chosen as representatives of the acoustic environmental conditions during CommsNet13 trials. As previously stated, one of the possible causes of the irregularly time-spaced acoustic fixes relies in the communication losses between the moored modems and the AUV due to acoustic channel effects. Since sound speed completely characterizes the channel properties (together with water and sea bottom geoacoustic parameters), the data pictured in figure 2.6 can be used to analyze the transmission quality between the moored modems and the moving USBL-vehicle, to better optimize the geometry of communication and therefore to possibly increase the reliability of acoustic fixes. This is precisely the main focus of the remaining chapters of this thesis.

[2]The reader should refer to [13] for an introduction on CTDs.

Chapter 3

Underwater Acoustics Fundamentals

The aim of this chapter is to introduce the unfamiliar reader to the basic concepts of underwater acoustics, in order to understand how computational methods work and to interpret the developments and the results provided in the following chapters.

Section 3.1 contains a brief summary of the main oceanographic physical quantities (especially sound speed), and how they influence sound propagation underwater. Acoustical properties of the ocean environment and the seabed are described too.

Section 3.2 presents some characteristic propagation paths of sound waves in underwater environments. Using the ray theory formalism, wave paths are a direct consequence of *Snell's Law*, which relates the ray angle to the local sound speed. If the speed of sound is not constant, the rays will follow curved paths rather than straight ones, and this has a great impact on sonar coverage and source-receiver transmissions.

Section 3.3 introduces the theory of acoustic waves. The wave equation in fluids is formulated both in the time and frequency domains, and the *principle of reciprocity* is stated. The former is the basis for the numerical methods described in Chapter 4, the latter is of fundamental practical importance in wave phenomena and linear systems.

The contents of this chapter were developed using books [14, 15] as the main reference materials. For a complete treatment on ocean acoustics, the reader should also refer to [16, 17].

3.1 The Underwater Acoustic Environment

3.1.1 Oceanographic and Physical Properties

The ocean is an acoustic waveguide limited above by the sea surface and below by the seafloor. The speed of sound (c) in the waveguide is the most important quantity and is normally related to density and compressibility. The sound speed is given by the square root of the ratio between volume stiffness (or bulk modulus) and density:

$$c = \sqrt{\frac{K}{\rho}}. \tag{3.1}$$

Both volume stiffness and density depend on the properties of the medium. Typical values for fresh water are $K = 2.25 \cdot 10^9$ Pa and $\rho = 1024$ Kg/m^3, which give a sound speed of $c = 1500$ m/s.

Usually, sound speed in water is calculated as an empirical function of three independent variables: temperature (T) in degrees centigrade, salinity (S) in parts per thousand[1], and depth (z) in meters. In the literature, there are several empirical formulas for calculating sound speed in water. For our purposes the following one is sufficiently accurate [19]:

$$c \;=\; 1448.6 + 4.618\,T - 0.0523\,T^2 + 1.25(S-35) + 0.017\,z. \qquad (3.2)$$

For normal environmental conditions and at 10 $^\circ C$ water temperature, the gradients are approximately:

$$\begin{aligned} \frac{\mathrm{d}c}{\mathrm{d}T} &= 3.5 \text{ m/s per } ^\circ\text{C}, \\ \frac{\mathrm{d}c}{\mathrm{d}S} &= 1.25 \text{ m/s per pro mille salt content}, \\ \frac{\mathrm{d}c}{\mathrm{d}z} &= 0.017 \text{ m/s per meter increasing depth}. \end{aligned}$$

Seasonal and diurnal changes affect the oceanographic parameters in the upper ocean, especially temperature. In addition, all these parameters are a function of geography. Even if the variation of the sound speed due to these fluctuations is relatively small, it has a significant effect on sound propagation.

A generic sound speed profile for an ocean environment is given in figure 3.1. This profile is characterized by a number of more or less distinct layers. Near the surface there is a layer where the temperature will be subject to daily or seasonal changes in heating or cooling as well as from the mixing of water masses as a result of ocean wave action. Just beneath this surface layer there may be a seasonally dependent thermocline, in which sound speed decreases with depth. In summer, the gradient is often steep as a result of warmer surface water, while in winter the effect is less pronounced. The gradient and the thickness of the layers mentioned above will vary according to geographical position, season, time of day, and meteorological conditions. Beneath these layers is the main thermocline, where the temperature decreases with depth with a gradient less affected by surface conditions. At great water depth, the temperature remains essentially constant, but the sound speed begins to increase with depth as a consequence of increasing pressure. This means that there is a depth where sound speed reaches a minimum, creating a sound channel where sound can be focused and concentrated (see Section 3.2.1). The axis of this channel will vary with the degree of latitude. In southern waters the axis will normally lie at about 1000 m depth, while in northern waters it will be shallower and in polar districts close to the surface (see Section 3.2.3).

The sound speed profile shown in figure 3.1 is typical for the northern Atlantic. As mentioned earlier, the temperature in the upper layers will strongly depend on the environmental conditions. Especially, wind and waves will sometimes cause a

[1]Salinity is expressed as a function of potassium chloride's conductivity (psu, Practical Salinity Scale [18]).

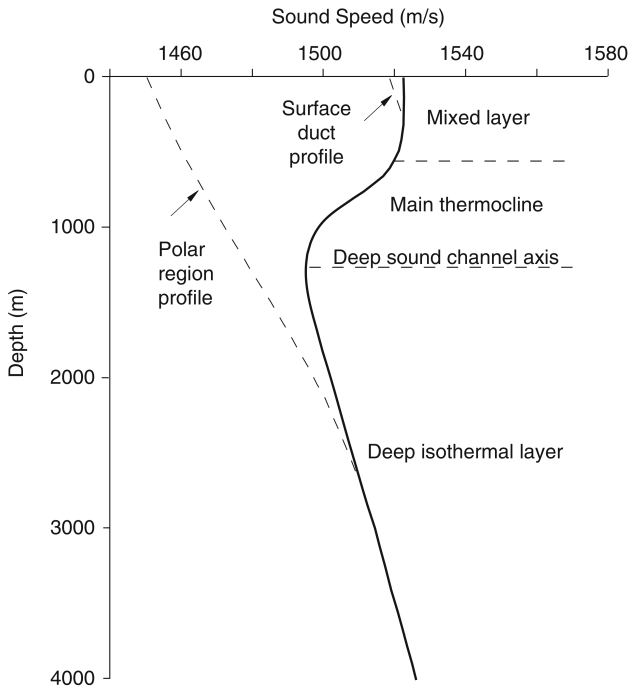

Figure 3.1: Typical sound speed profile as a function of depth for an ocean environment (adapted from [14]).

total mixing of the water masses, making the water temperature almost constant in the surface layer. In such a mixed layer with constant temperature, sound speed will have a small positive gradient because of the depth.

Turning to the upper and lower boundaries of the ocean waveguide, the sea surface is a simple horizontal boundary and a nearly perfect reflector. The seafloor, on the other hand, is a lossy boundary with strongly varying topography across ocean basins (see Section 3.1.3).

3.1.2 Relevant Units in Ocean Acoustics

Underwater acoustic signals are *compressional waves* (or *longitudinal waves*) propagating in a fluid medium, in which the displacement of the medium is in the same direction as, or the opposite direction to, the direction of travel of the wave[2]. The main physical quantities that characterize this type of wave are *pressure* (which is a function of space and time), expressed in pascals (Pa = N/m^2), and *intensity*, expressed in W/m^2; the latter is defined as the average rate of flow of energy through a unit area that is normal to the direction of propagation, and it has the following expression:

$$I = \frac{p_{rms}^2}{Z}, \tag{3.3}$$

where p_{rms} is the root mean square sound pressure, i.e. the squared integral of instantaneous pressure over a time period T, and $Z = \rho c$ is the *acoustic impedance*

[2]There are also *transverse waves*, or *shear waves*, in which the displacement of the medium is perpendicular to the direction of propagation of the wave.

of the medium, measured in Kg/(m^{2}s). For seawater, Z is $1.5 \cdot 10^6$ Kg/(m^{2}s).

The *decibel* (dB) is the dominant adimensional unit in underwater acoustics and denotes a ratio of intensities expressed in terms of a logarithmic (base 10) scale:

$$10 \log \left(\frac{I_1}{I_2} \right) \; = \; 20 \log \left(\frac{p_1}{p_2} \right), \tag{3.4}$$

where the transition from intensities to *rms* pressures assumes that the acoustic impedance doesn't change (so that the intensity in a plane wave becomes proportional to the square of the pressure amplitude). Absolute intensities can therefore be expressed by using a reference intensity. The presently accepted reference intensity I_0 is the intensity of a plane wave having a p_{rms} equal to 1 μPa $=$ 10^{-6} Pa; therefore, in seawater, we have $I_0 = 0.67 \cdot 10^{-18}$ W/m^2 (i.e. 0 dB re 1μPa).

An acoustic signal traveling through the ocean becomes distorted due to multipath effects and weakened due to various loss mechanisms. The standard measure in underwater acoustics of the change in signal strength with range is *transmission loss* (TL) defined as the ratio in decibels between the acoustic intensity $I(r, z)$ at a field point and the intensity I_0 at 1-m distance from the source:

$$\begin{aligned} \text{TL} \; &= \; -10 \log \left(\frac{I(r,z)}{I_0} \right) \\ &= \; -20 \log \left(\frac{|p(r,z)|}{|p_0|} \right) \qquad \text{dB re 1 m}, \end{aligned} \tag{3.5}$$

where the minus sign makes it positive, since $I(r, z) < I_0$. Again, the last equation assumes that the acoustic impedance at the field point is the same as that at the source, assumption that will remain valid throughout this document.

Transmission loss may be considered to be the sum of a loss due to *geometrical spreading* and a loss due to *attenuation*. The spreading loss is simply a measure of the signal weakening as it propagates outward from the source. It can be of two types:

- *Spherical spreading loss*, when the power radiated by the source is equally distributed over the surface area of a sphere surrounding the source;
- *Cylindrical spreading loss*, when the medium has plane upper and lower boundaries.

For a point source in a waveguide with depth D and range r, we have spherical spreading in the nearfield ($r \leq D$) followed by a transition region toward cylindrical spreading which applies only at longer ranges ($r \gg D$).

During their propagation, acoustic waves will also encounter losses caused by viscosity, thermal conductance, and different relaxation phenomena. Ultimately, the acoustic energy is lost to heat due to the interaction of the particles of the medium caused by the waves. A very important parameters is the *absorption coefficient* (or *attenuation coefficient*) α, which is defined from a decay-law-type differential equation in theoretical acoustics:

$$\frac{\mathrm{d}A}{\mathrm{d}x} \; = \; -\alpha \Rightarrow A \; = \; A_0 e^{-\alpha x}, \tag{3.6}$$

Bottom Type	p (%)	ρ_b/ρ_w -	c_p/c_w -	c_p (m/s)	c_s (m/s)	α_p dB/λ_p	α_s dB/λ_s
Clay	70	1.5	1.00	1500	<100	0.2	1.0
Silt	55	1.7	1.05	1575	150	1.0	1.5
Sand	45	1.9	1.10	1650	300	0.8	2.5
Gravel	35	2.0	1.20	1800	500	0.6	1.5
Moraine	25	2.1	1.30	1950	600	0.4	1.0
Chalk	-	2.2	1.60	2400	1000	0.2	0.5
Limestone	-	2.4	2.00	3000	1500	0.1	0.2
Basalt	-	2.7	3.50	5250	2500	0.1	0.2

$c_w = 1500$ m/s, $\rho_w = 1000$ kg/m^3

Table 3.1: Geoacoustic properties for sediments and other materials.

where A_0 is the *rms* amplitude of the wave at $x = 0$. This coefficient is a function of frequency and it is usually expressed in dB/km or dB/λ (λ is the wavelength).

A quantitative understanding of acoustic loss mechanisms in the ocean is required for the modeling of sound propagation. The most important loss mechanisms are volume attenuation, bottom reflection loss, and boundary and volume scattering. For a complete treatment of these mechanisms, see [14, pagg. 35-57].

3.1.3 Sound Speed in Marine Sediments

When sound interacts with the seafloor, the structure of the ocean bottom becomes important. Ocean bottom sediments are often modeled as fluids, which means that they support only one type of sound wave - a compressional wave. This is often a good approximation since the rigidity of the sediment is usually considerably less than that of a solid, such as rock. In the latter case, which applies to the ocean basement or the case where there is no sediment overlying the basement, the medium must be modeled as elastic, which means it supports both compressional and shear waves[3].

A *geoacoustic model* is defined as a model of the real seafloor with emphasis on measured, extrapolated, and predicted values of those material properties important for the modeling of sound transmission. The information required for a complete geoacoustic model should include at least the following depth-dependent material properties: the compressional wave speed c_p, the shear wave speed c_s, the compressional wave attenuation α_p, the shear wave attenuation α_s, and the density ρ. Moreover, information on the variation of all of these parameters with geographical position is required.

The geoacoustic properties of some typical seafloor materials are listed in table 3.1. Several observations can be made. First, we see that the porosity p relates in a simple fashion to the material density and the wave speed, i.e. a lower porosity results in a higher density and higher wave speeds. Next, the shear speeds in unconsolidated sediments (clay, silt, sand, gravel) increase rapidly with depth be-

[3]In reality, the media are viscoelastic, meaning that they are also lossy.

low the water-bottom interface[4]. Wave attenuations α are generally given in units of dB per wavelength, indicating that the attenuation increases linearly with frequency. Bottom materials are three-to-four orders of magnitude more lossy than seawater. It must be emphasized that these values are merely indicative. The vastly different material compositions and stratifications encountered in the ocean seafloors essentially mean that a specific geoacoustic model must be established for any given (small or large) geographical area. Clearly, the construction of a detailed geoacoustic model for a particular ocean area is a tremendous task, and the amount of approximate (or inaccurate) information included is the primary limiting factor on the accurate modeling of bottom-interacting sound transmission in the ocean.

3.2 Underwater Sound Propagation

All the typical sound paths resulting from various sound speed profiles can be understood from *Snell's Law*, which states that:

$$\frac{\cos\theta}{c} = \text{const}, \tag{3.7}$$

and relates the ray angle (w.r.t. the horizontal) θ to the local sound speed c. It is quite straightforward to see that the implication of this law is that sound bends locally towards regions of low sound speed: if c increases, θ must decrease to compensate the variation, and vice versa.

In this section we are going to describe four typical environmental situations and characteristic paths: deep sound channel, convergence-zone, arctic propagation and shallow waters. We must remember that the modeling of sound propagation is complicated because the environment varies laterally (it is *range dependent*) and all environmental effects on sound propagation are dependent on acoustic frequency in a rather complicated way.

3.2.1 Deep Sound Channel

As we can see from figure 3.2, the principal characteristic of standard deep-water propagation is the existence of an upward-refracting sound-speed profile which permits long-range propagation without significant bottom interaction (*deep sound channel*). Typical deep-water environments are found in all oceans at depths exceeding 2000 m.

Propagation in the deep sound channel, also referred to as the SOFAR channel, allows long-range propagation without encountering reflection losses at the sea surface or the seafloor. Because of the low transmission loss, acoustic signals in the deep sound channel have been recorded over distances of thousands of kilometers.

The sound channel axis (minimum sound speed) varies in depth from around 1000 m at mid-latitudes to the ocean surface in polar region; a necessary condition for the existence of low-loss refracted paths is that the sound-speed axis is below

[4]Shear speeds in sediments are therefore most appropriately given in terms of their depth dependence.

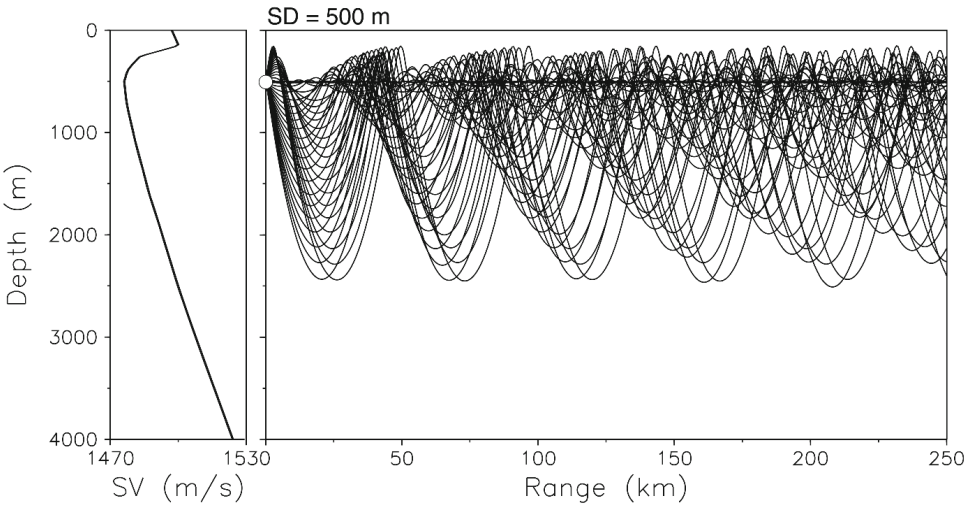

Figure 3.2: Deep sound channel propagation (adapted from [14]).

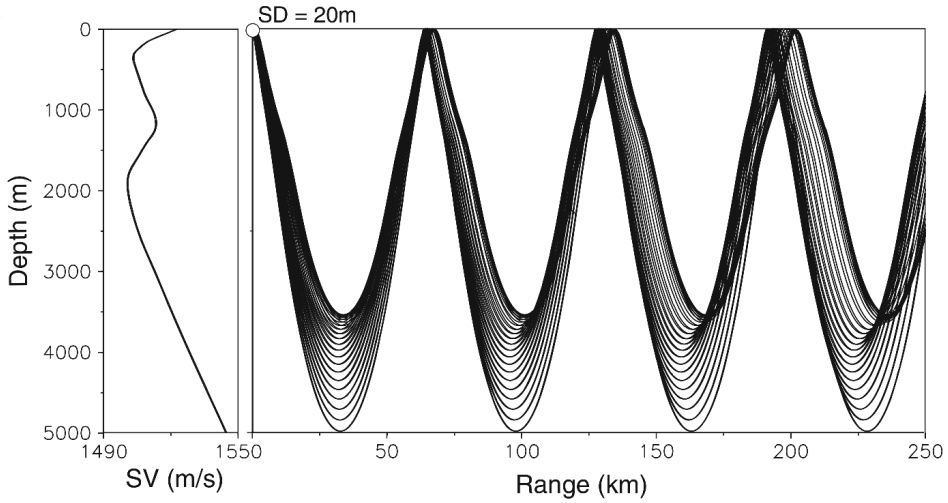

Figure 3.3: Convergence-zone propagation (adapted from [14]).

the sea surface, since otherwise propagation becomes entirely surface-interacting and lossy (see Section 3.2.3).

3.2.2 Convergence Zones

The acoustic field pattern shown in figure 3.3 is one of the most interesting features of propagation in the deep ocean. The presence of two sound channel axes (a sort of double SOFAR) determines a new propagation path. This pattern is referred to as *convergence-zone* (CZ) propagation because the sound emitted from a near-surface source forms a downward-directed beam which, after following a deep refracted path in the ocean, reappears near the surface to create a zone of high sound intensity (convergence or focusing) at a distance of kilometers from the source. The phenomenon is repetitive in range, with the distance between the

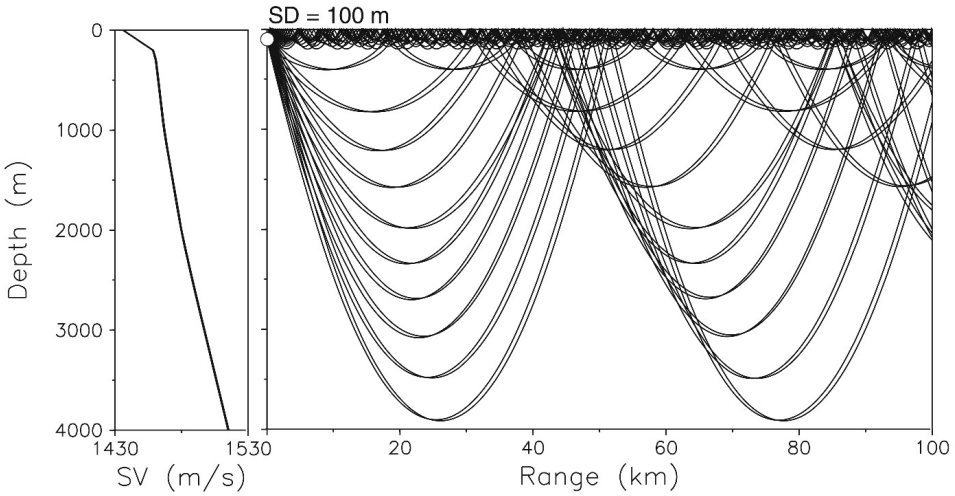

Figure 3.4: Arctic environment propagation (adapted from [14]).

high-intensity regions called the *convergence-zone range*.

The importance of convergence-zone propagation stems from the fact that it allows for long-range transmission of acoustic signals of high intensity and low distortion. The convergence zones are spaced approximately 65 km apart, note also that the convergence zone width increases with zone number; the second zone is wider than the first, and so on, until eventually at several hundreds kilometers the zones overlap and become indistinguishable.

The paper [20] was the first to address in detail the environmental conditions for the existence of convergence zones and attempted a theoretical description of the convergence-zone structure using ray theory.

3.2.3 Arctic Propagation

Propagation in the Arctic Ocean (figure 3.4) is characterized by an upward refracting profile over the entire water depth causing energy to undergo repeated reflections at the underside of the ice. The sound speed profile in these regions can often be approximated by two linear segments with a steep gradient in the upper 200 m caused both by the increase in temperature and in salinity with depth.

The ray diagram in figure 3.4 shows that energy is partly channeled beneath the ice cover within the 200 m deep surface duct (since minimum sound speed is at the surface) and partly follows deeper refracted paths. All rays within a cone of almost $\pm 17^\circ$ propagate to long ranges without bottom interaction. This type of propagation is known to degrade rapidly with increasing frequency above 30 Hz (for more details see [17]).

3.2.4 Shallow Waters

The principal characteristic of shallow waters propagation is that the sound speed profile is downward refracting or nearly constant over depth, meaning that long-range propagation takes place exclusively via bottom-interacting paths (as one

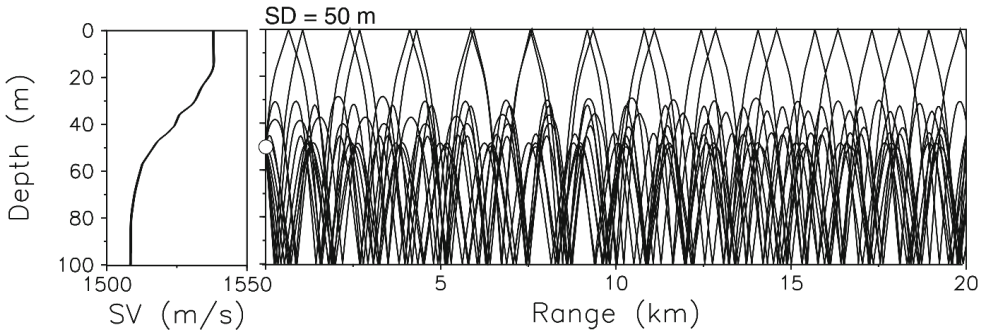

Figure 3.5: Shallow waters propagation (adapted from [14]).

would expect). Typical shallow waters environments are found on the continental shelf for water depths down to 200 m.

Accurate prediction of long-range propagation in shallow waters is a very complex problem. In shallow waters the surface, volume and bottom properties are all important, are spatially and temporally varying, and the parameters are generally not known in sufficient detail and with enough accuracy to permit long-range predictions in a satisfactory way.

A ray picture of propagation in a 100 m deep shallow waters duct is shown in figure 3.5. The sound speed profile is typical of the Mediterannean Sea in the summer. There is a warm surface layer causing downward refraction and hence repeated bottom interaction for all ray paths. The seasonal variation in sound speed structure is significant with winter conditions being nearly isospeed. The result is that there is less bottom interaction in winter than in summer, which means that propagation conditions are generally better in winter than in summer.

To better examine transmission loss variability in shallow water propagation, see [14, pagg. 28-32].

3.3 Acoustic Waves Theory

Acoustic waves are mechanical vibrations. When an acoustic wave passes through a medium, it causes local density changes that are related to local displacements of mass about the rest positions of the particles in the medium. This displacement leads to the formation of forces that act to restore the density to the equilibrium state and move the particles back to their rest positions. The medium may be a gas, liquid, or solid material. The basic equations of acoustics are obtained by considering the equations for an inviscid and compressible fluid. These equations are expressed with the notation that p is the pressure, ρ is density, S is entropy, and $\boldsymbol{v}$ is particle velocity (bold face letters denote vectors).

3.3.1 Derivation of the Wave Equation

We now formulate the wave equation describing acoustic waves in fluids, using three simple principles:

- The momentum equation, also known as Euler's equation.
- The continuity equation, or conservation of mass.
- The equation of state: the relationship between changes in pressure and density or volume.

We consider a small rectangular volume element with sides $\mathrm{d}x$, $\mathrm{d}y$ and $\mathrm{d}z$, volume $V = \mathrm{d}x\,\mathrm{d}y\,\mathrm{d}x$ and mass ρV, with ρ being the density of the fluid. As a result of the acoustic wave action, mass will alternately flow into and out of the element with displacement velocity, or particle velocity, $\boldsymbol{v} = [v_x\ v_y\ v_z]$, depending on the position of the element and the time.

Conservation of mass implies that the net changes in the mass, which result from its flow through the element, must be equal to the changes in the density of the mass of the element. This is expressed by the *continuity equation*:

$$\frac{\partial \rho}{\partial t} = -\nabla \cdot (\rho \boldsymbol{v}). \tag{3.8}$$

Equation (3.8) is nonlinear since it contains the product of density and particle velocity, both being functions of time and position.

The second fundamental equation is *Euler's equation* (or *momentum balance*):

$$\rho \left[\frac{\partial \boldsymbol{v}}{\partial t} + \boldsymbol{v} \cdot \nabla \boldsymbol{v} \right] = -\nabla p, \tag{3.9}$$

and it is an extension of Newton's second law, which states that force equals the product of mass and acceleration. The extension is the second left-hand term in equation (3.9), which represents the change in velocity with position for a given time instant, while the first term describes the change with time at a given position.

Finally, an equation of state is required to give a relationship between a change in density and a change in pressure, taking into consideration the existing thermodynamic conditions. The equation of state may be formulated as pressure as a function of density and entropy S:

$$p = p(\rho, S) \Rightarrow p = p(\rho). \tag{3.10}$$

In a real fluid, the dissipation processes like viscosity and thermal conduction act to increase the entropy, as demanded by the second law of thermodynamics. The increase in entropy is associated with heating of the fluid as the sound wave passes and a corresponding decrease in the energy of the sound wave. The effect of an increase of entropy leads naturally to the idea of attenuation of the sound.

Equations (3.8) to (3.10) can be linearized by assuming that each physical quantity is a function of a steady state, time-independent value and a small fluctuation term:

$$\begin{aligned} p &= p_0 + p', \\ \rho &= \rho_0 + \rho', \\ \boldsymbol{v} &= \boldsymbol{v}_0 + \boldsymbol{v}'. \end{aligned} \tag{3.11}$$

The variables p', ρ' and $\boldsymbol{v}'$ are functions of time and spatial positions; the variables p_0, ρ_0 and $\boldsymbol{v}_0$ are independent of time, but may be functions of spatial positions. We also assume that there is also no mean flow, that is, $\boldsymbol{v}_0 = 0$. We expand equation (3.10) about the equilibrium values, indicated by the subscript 0, and obtain:

$$p = p_0 + \left[\frac{\partial p}{\partial \rho}\right]_0 (\rho - \rho_0) + \frac{1}{2}\left[\frac{\partial^2 p}{\partial \rho^2}\right]_0 (\rho - \rho_0)^2 + \dots \tag{3.12}$$

Using equations (3.11) and (3.12), after some passages[5] and assuming that nominal density ρ_0 is constant in space, we obtain the acoustic wave equation for sound pressure:

$$\nabla^2 p' - \frac{1}{c_0^2}\frac{\partial^2 p'}{\partial t^2} = 0, \tag{3.13}$$

where ∇^2 is the Laplacian operator and c_0 is the sound speed at the ambient conditions, calculated from equation (3.1).

Other variables, such as particle velocity, also must satisfy the same wave equation. For instance, the wave equation for particle velocity $\mathbf{v}$ is

$$\nabla(\nabla \cdot \boldsymbol{v}) - \frac{1}{c_0^2}\frac{\partial^2 \boldsymbol{v}}{\partial t^2} = 0. \tag{3.14}$$

Generally, it is more convenient to describe the wave by means of scalar variables. Denoting the velocity potential as ϕ, the particle velocity is expressed by the gradient of the velocity potential ϕ as:

$$\boldsymbol{v} = \nabla\phi. \tag{3.15}$$

By combining equation (3.15) with equation (3.14), we find that the velocity potential satisfies the wave equation:

$$\nabla^2 \phi - \frac{1}{c_0^2}\frac{\partial^2 \phi}{\partial t^2} = 0. \tag{3.16}$$

It follows that the sound pressure is equal to:

$$p = -\rho_0 \frac{\partial \phi}{\partial t}. \tag{3.17}$$

Equations (3.15) to (3.17) are the ones generally applied in further treatments of wave propagation.

The wave equations that were formulated hitherto may be referred to as *homogeneous wave equations* because they lack a source term. Introduction of a source term leads to the *inhomogeneous wave equations*. A source can be an external force or an injection of a volume of fluid (i.e. injection of new mass into the medium). The pressure wave equation with a volume source term is expressed as:

$$\nabla^2 p' - \frac{1}{c_0^2}\frac{\partial^2 p'}{\partial t^2} = \rho_0 \frac{\partial f(\boldsymbol{r}, t)}{\partial t}, \tag{3.18}$$

where $f(\boldsymbol{r}, t)$ is the forcing term for a source located at $\boldsymbol{r}$, and the velocity potential equation becomes:

$$\nabla^2 \phi - \frac{1}{c_0^2}\frac{\partial^2 \phi}{\partial t^2} = -f(\boldsymbol{r}, t). \tag{3.19}$$

[5]For all the details see [15, pagg. 16-18].

3.3.2 The Helmholtz Equation

We can move from time domain to frequency domain by using the Fourier transform:

$$\Phi(\omega) \;=\; \int_{-\infty}^{+\infty} \phi(t) \mathrm{e}^{i\omega t}\, \mathrm{d}t, \tag{3.20}$$

and back to time domain by using the inverse transform:

$$\phi(t) \;=\; \frac{1}{2\pi} \int_{-\infty}^{+\infty} \Phi(\omega) \mathrm{e}^{-i\omega t}\, \mathrm{d}\omega. \tag{3.21}$$

Analysis in the frequency domain means that we assume a solution of the wave equation in the form $\Phi(\omega)\exp(i\omega t)$. After this solution is found, the solution in the time domain, and consequently the time response, is found by using the inverse transformation in equation (3.21).

The inhomogeneous wave equation for the velocity potential may then be expressed as:

$$\left[\nabla^2 + \kappa^2(\mathbf{r})\right] \Phi(\mathbf{r}, \omega) \;=\; -F(\boldsymbol{r}, \omega), \tag{3.22}$$

where $F(\boldsymbol{r}, \omega)$ is the Fourier transform of $f(\boldsymbol{r}, t)$ defined in equation (3.18), and the wave number $\kappa(\boldsymbol{r})$ is defined as:

$$\kappa(\boldsymbol{r}) \;=\; \frac{\omega}{c_0(\boldsymbol{r})}. \tag{3.23}$$

Equation (3.22) is the wave equation in the frequency domain and is also referred to as the *inhomogeneous Helmholtz equation*, which is often easier to solve than the corresponding wave equation in the time domain due to the reduction in the dimension of this PDE (partial differential equation). This simplification is achieved at the cost of having to evaluate the inverse Fourier transform (3.21).

The Helmholtz equation, rather than the wave equation, form the theoretical basis for the most important numerical methods in computational acoustics, including Wavenumber Integration (WI), Normal Modes (NM) and Parabolic Equations (PE) [14]. In spite of the relative simplicity of equation (3.22), there is no universal solution technique available. The solution technique that can be applied depends on the following factors:

- Dimensionality of the problem.
- Medium wavenumber variation $\kappa(\boldsymbol{r})$, i.e. the sound speed variation $c(\boldsymbol{r})$.
- Boundary conditions.
- Source-receiver geometry.
- Frequency and bandwidth.

3.3.3 The Principle of Reciprocity

Reciprocity is a fundamental principle related to wave propagation and to linear systems in general. It is therefore of great practical importance. Applied to wave propagation, the reciprocity principle enables us to switch the positions of source and receiver and still receive the same acoustic signal.

Let's consider an ideal experimental situation with transmission of sound between two positions indicated by A and B. In one experiment sound is transmitted from A by a small spherical sound source with strength[6] Q_A and we measure the sound pressure p_B in position B. Another experiment uses a source at position B with strength Q_B and we receive the pressure p_A at position A.

The *reciprocity principle* states that the ratios of source strengths and received pressures are the same, as expressed by the following relationship:

$$\frac{Q_A}{p_B} = \frac{Q_B}{p_A}. \tag{3.24}$$

Equation (3.24) is very general and applies as long as the sources have the same frequency. The equation constitutes the reciprocity principle: the pressure at position B due to a source at position A is equal to the pressure at A due to a similar source at position B. This result holds also for the case where the medium is composed of several regions, and in cases where the wave undergoes reflections and refractions on its path from A to B or vice versa.

[6]The *source strength* $Q(\omega)$ is the Fourier transform of the source function in equation (3.19) [15].

Chapter 4

Sound Propagation Models

Sound propagation in the ocean is mathematically described by the wave equation, whose parameters and boundary conditions are representative of the ocean environment. There are essentially five types of models (computer solutions to the wave equation) to describe sound propagation in the sea: spectral or "fast field program" (FFP), normal modes (NM), ray tracing and parabolic equation (PE) models, and direct finite-difference (FDM), or finite element (FEM) solutions to the full wave equation. All of these models permit the ocean environment to vary with depth; a model that also permits horizontal variations in the environment is termed *range dependent*. The major difference between the various techniques is the mathematical manipulation of equation (3.19) being applied before actual implementation of the solution, another difference is the form of the wave equation used.

FDM and FEM are the most direct, general approaches, but their importance in ocean acoustics is rather limited due to excessive computational requirements. The alternative numerical approaches (FFP, NM, PE and rays) are much more tractable in term of numerical requirements and are therefore in more widespread use in the ocean acoustics community. However, the improved efficiency is obtained at the cost of generality. All these approaches are based on assumptions allowing for simplifying mathematical manipulations of the wave equation.

This chapter describes one of these models, ray tracing (Section 4.1), which was used to produce all the acoustic channel simulations shown in this thesis. Section 4.2 is a brief summary of the available software that implements this method.

The contents of this chapter were developed using books [14, 15], together with [21, 22], as the main reference materials.

4.1 Ray Methods

Ray acoustics and ray-tracing techniques are the most intuitive and often the simplest means for modeling sound propagation in the sea. Ray acoustics is based on the assumption that sound propagates along rays that are normal to wave fronts, surfaces of constant phase of the acoustic waves. The computational technique known as ray tracing is a method used to calculate the trajectories of the ray paths of sound from the source.

The ray theory approach is essentially a high-frequency approximation, applicable to frequencies for which the wavelength is much smaller than the water depth and, in addition, much smaller than the characteristic distance of variation in the sound speed. This method is sufficiently accurate that it is used in applications involving echo sounders, sonar, and communication systems for short and medium-short distances. These devices normally use frequencies that satisfy the high-frequency conditions.

Ray theory gives a good physical picture of how sound propagates in inhomogeneous media. An advantage of ray theory is that ray characteristics are not functions of frequency and therefore are very efficient for modeling propagation of broadband time signals. Section 4.1.1 introduces ray acoustics theory, which is the fundamental basis upon which practical implementations are built, while Section 4.1.2 describes the differences between coherent and incoherent transmission loss, which is a fundamental distinction for this kind of methods. Section 4.1.3 lists some of the typical artifacts and issues that can be encountered in ray acoustics.

4.1.1 Theory of Ray Acoustics

The wave equation for the velocity potential in rectangular (or cartesian) coordinates $\boldsymbol{x} = (x, y, z)$ may be written as:

$$\nabla^2\phi(x,y,z,t) \;=\; \frac{1}{c^2(x,y,z)}\frac{\partial^2\phi(x,y,z,t)}{\partial t^2}. \tag{4.1}$$

We assume a solution of the form:

$$\phi(x,y,z,t) \;=\; A(x,y,z)\exp\left[-i\omega\left(t-\frac{W(x,y,z)}{c_0}\right)\right], \tag{4.2}$$

where $A(x,y,z)$ is the position-dependent amplitude and c_0 is a reference sound speed. The function $W(x,y,z)$ represents the wave fronts because all points in space where $W(x,y,z) - c_0 t$ is a constant have the same phase, as can be seen by examining the exponential in equation (4.2).

Inserting equation (4.2) into the wave equation (4.1), and requiring the wave equation to be satisfied independently for both the real and the imaginary parts results in two equations from which we can determine $W(x,y,z)$ and $A(x,y,z)$:

$$\nabla^2 A - A\frac{\omega^2}{c_0^2}\nabla W\cdot\nabla W \;=\; -A\frac{\omega^2}{c^2}, \tag{4.3}$$

$$2\nabla A\cdot\nabla W + A\nabla^2 W \;=\; 0. \tag{4.4}$$

So far, no assumptions have been made, and in principle we can solve these two differential equations, thereby finding a complete solution for wave equations that have three-dimensional variation in the sound speed $c(x,y,z)$. This approach is often referred to as *exact ray tracing*. In practice, this approach is very difficult because equations (4.3) and (4.4) are nonlinear and coupled. Therefore some simplifying assumptions must be introduced. If we assume that:

$$\nabla^2 A \ll A\frac{\omega^2}{c^2}, \tag{4.5}$$

the second term on the left side of equation (4.3) dominates, and the first term can be neglected. This mean that the wave front W must satisfy the equation:

$$\nabla W \cdot \nabla W \;=\; \left(\frac{c_0}{c}\right)^2, \tag{4.6}$$

which can be rewritten as:

$$\nabla W^2 \;=\; n^2. \tag{4.7}$$

Here, the index of refraction n is defined as:

$$n \;=\; \frac{c_0}{c}. \tag{4.8}$$

Equation (4.7), the so called *eikonal equation*, is a first-order nonlinear differential equation; it gives the geometry for the spatial variation of the wave front $W(x, y, z, t)$. Equation (4.4), the *transport equation*, gives the sound field amplitude as a function of spatial position.

Two conditions must be satisfied for the assumption made in equation (4.5) to be valid. First, the frequency must be sufficiently high that any variation in the sound speed over a distance equal to a wavelength is vanishingly small; this is the reason why ray methods are rarely applied to low-frequency problems. Second, the spatial variation of the amplitude must be small, which means that equation (4.5) will not be satisfied at the edges of a sound field. A consequence of this second condition is that diffraction effects are not well represented by the ray approximation.

We now continue with the eikonal equation to calculate the trajectories of the ray paths. We first define the unit vector $\boldsymbol{e}$ normal to the wave front $W(x, y, z, t)$; from equation (4.7), we find that:

$$\nabla W \;=\; ne. \tag{4.9}$$

Although the solution of this equation defines the ray path direction at any point on the trajectory, it is more convenient to work with the ray path coordinates $\boldsymbol{s}(x, y, z)$, which determine the ray direction $\boldsymbol{e}$ by:

$$\boldsymbol{e} \;=\; \frac{\mathrm{d}\boldsymbol{s}}{\mathrm{d}s} \;=\; \boldsymbol{i}\frac{\mathrm{d}x}{\mathrm{d}s} + \boldsymbol{j}\frac{\mathrm{d}y}{\mathrm{d}s} + \boldsymbol{k}\frac{\mathrm{d}z}{\mathrm{d}s}, \tag{4.10}$$

where $\mathrm{d}x/\,\mathrm{d}s$, $\mathrm{d}y/\,\mathrm{d}s$ and $\mathrm{d}z/\,\mathrm{d}s$ are the direction cosines of the ray and have the property:

$$\left(\frac{\mathrm{d}x}{\mathrm{d}s}\right)^2 + \left(\frac{\mathrm{d}y}{\mathrm{d}s}\right)^2 + \left(\frac{\mathrm{d}z}{\mathrm{d}s}\right)^2 \;=\; 1, \tag{4.11}$$

where s is the distance measured along the ray path.

The direction numbers for the normal to the phase front of $W(x, y, z, t)$ are $\partial W/\partial x$, $\partial W/\partial y$ and $\partial W/\partial z$ for the x, y and z directions, respectively. These are proportional to the direction cosines and the proportionality may be expressed by

three equations:

$$\begin{aligned} \frac{\mathrm{d}x}{\mathrm{d}s} &= a\frac{\mathrm{d}W}{\mathrm{d}x}, \\ \frac{\mathrm{d}y}{\mathrm{d}s} &= a\frac{\mathrm{d}W}{\mathrm{d}y}, \\ \frac{\mathrm{d}z}{\mathrm{d}s} &= a\frac{\mathrm{d}W}{\mathrm{d}z}. \end{aligned} \tag{4.12}$$

The value of a, after some passages, is found to be equal to $1/n$, therefore equations (4.12) become:

$$\begin{aligned} \frac{\mathrm{d}x}{\mathrm{d}s} &= \frac{1}{n}\frac{\mathrm{d}W}{\mathrm{d}x}, \\ \frac{\mathrm{d}y}{\mathrm{d}s} &= \frac{1}{n}\frac{\mathrm{d}W}{\mathrm{d}y}, \\ \frac{\mathrm{d}z}{\mathrm{d}s} &= \frac{1}{n}\frac{\mathrm{d}W}{\mathrm{d}z}. \end{aligned} \tag{4.13}$$

To find the equation describing the ray path $\mathbf{s}(x, y, z)$, we must eliminate $W(x, y, z, t)$ by taking the differential $\mathrm{d}/\,\mathrm{d}s$ along the path. For the x-component, this produces:

$$\frac{\mathrm{d}}{\mathrm{d}s}\left(n\frac{\mathrm{d}x}{\mathrm{d}s}\right) = \frac{\mathrm{d}}{\mathrm{d}s}\left(\frac{\partial W}{\partial x}\right) = \frac{\partial}{\partial x}\left[\frac{\partial W}{\partial x}\frac{\mathrm{d}x}{\mathrm{d}s} + \frac{\partial W}{\partial y}\frac{\mathrm{d}y}{\mathrm{d}s} + \frac{\partial W}{\partial z}\frac{\mathrm{d}z}{\mathrm{d}s}\right]. \tag{4.14}$$

By using equations (4.7) and (4.11), this expression can be written as:

$$\frac{\mathrm{d}}{\mathrm{d}s}\left(n\frac{\mathrm{d}x}{\mathrm{d}s}\right) = \frac{\partial n}{\partial x}. \tag{4.15}$$

After similar treatment of the y- and z-components, we obtain:

$$\begin{aligned} \frac{\mathrm{d}}{\mathrm{d}s}\left(n\frac{\mathrm{d}x}{\mathrm{d}s}\right) &= \frac{\partial n}{\partial x}, \\ \frac{\mathrm{d}}{\mathrm{d}s}\left(n\frac{\mathrm{d}y}{\mathrm{d}s}\right) &= \frac{\partial n}{\partial y}, \\ \frac{\mathrm{d}}{\mathrm{d}s}\left(n\frac{\mathrm{d}z}{\mathrm{d}s}\right) &= \frac{\partial n}{\partial z}. \end{aligned} \tag{4.16}$$

In electromagnetics and optics, the speed of light in a vacuum is a fundamental quantity and thus is a natural choice for the reference speed c_0. In acoustics, there is no such fundamental reference speed. Therefore equation (4.16) is often expressed by using the sound speed as:

$$\begin{aligned} \frac{\mathrm{d}}{\mathrm{d}s}\left(\frac{1}{c}\frac{\mathrm{d}x}{\mathrm{d}s}\right) &= -\frac{1}{c^2}\frac{\partial c}{\partial x}, \\ \frac{\mathrm{d}}{\mathrm{d}s}\left(\frac{1}{c}\frac{\mathrm{d}y}{\mathrm{d}s}\right) &= -\frac{1}{c^2}\frac{\partial c}{\partial y}, \\ \frac{\mathrm{d}}{\mathrm{d}s}\left(\frac{1}{c}\frac{\mathrm{d}z}{\mathrm{d}s}\right) &= -\frac{1}{c^2}\frac{\partial c}{\partial z}. \end{aligned} \tag{4.17}$$

Equations (4.16) and (4.17) are ordinary differentials equations that describe how to compute ray trajectories in the general case where the sound speed $c(x, y, z)$ varies with all three spatial coordinates. In practice, this form is rarely used because of its complexity and the lack of detailed knowledge about the sound speed in the horizontal directions.

The next approximation involves assumption of *transverse isotropy* (TI), which means the sound speed may vary with depth z and range r, but not with azimuth. This assumption is also justified physically because the gradients in the ocean variables that affect sound speed (temperature and salinity) are much greater in depth than in x and y, as discussed in Section 3.1.1.

In this case we have cylindrical symmetry around the z axis and we therefore use cylindrical coordinates. A small segment of a ray path $\mathrm{d}s$ has horizontal and vertical components $\mathrm{d}r$ and $\mathrm{d}z$, respectively, and forms an angle (often called *grazing angle*) of θ with respect to the horizontal. With this cylindrical coordinates, we also introduce two new variables, called the ray parameters, $\xi(s)$ and $\zeta(s)$, defined as:

$$\begin{aligned} \xi(s) &= \frac{1}{c}\frac{\mathrm{d}r}{\mathrm{d}s} = \frac{1}{c}\cos\theta, \\ \zeta(s) &= \frac{1}{c}\frac{\mathrm{d}z}{\mathrm{d}s} = \frac{1}{c}\sin\theta. \end{aligned} \tag{4.18}$$

Parameters $\xi(s)$ and $\zeta(s)$ are proportional to the horizontal (k) and vertical (γ) wavenumber components, respectively, that is:

$$\begin{aligned} k &= \omega\xi, \\ \gamma &= \omega\zeta. \end{aligned} \tag{4.19}$$

By equations (4.17), the wavenumber components satisfy the differential equations:

$$\begin{aligned} \frac{\mathrm{d}\xi}{\mathrm{d}s} &= -\frac{1}{c^2}\frac{\partial c}{\partial r}, \\ \frac{\mathrm{d}\zeta}{\mathrm{d}s} &= -\frac{1}{c^2}\frac{\partial c}{\partial z}. \end{aligned} \tag{4.20}$$

Using equation (4.18), we find that the initial values for integrating those equations are:

$$\begin{aligned} \xi &= \frac{\cos\theta_0}{c(r_0, z_0)}, \\ \zeta &= \frac{\sin\theta_0}{c(r_0, z_0)}. \end{aligned} \tag{4.21}$$

where θ_0 is the ray angle and $c(r_0, z_0)$ is the sound speed at the starting point (r_0, z_0).

Equations (4.20) determine the change in ray path direction as the sound speed changes with both range and depth. These equations are therefore the basis for ray tracing in a range dependent environment, where the sound speed is a function of both range and depth. In principle, equations (4.20) can be integrated when we know the sound speed at all positions in space. The starting values of the integration are given by the initial direction of the ray at the source and the sound speed at the source, as indicated in equations (4.21).

4.1.2 Transmission Loss Calculation

Every single ray path has its own pressure associated. The pressure field at any point then involves identifying all the *eigenrays*, that is, the rays which pass through that point. Each eigenray makes a contribution to the complex pressure field based on its intensity and phase at that point. The intensity is calculated by simply summing up the contributions of each of the eigenrays leading to:

$$p^{(C)}(r,z) \;=\; \sum_{j=1}^{N(r,z)} p_j(r,z), \tag{4.22}$$

where $N(r,z)$ denotes the number of eigenrays contributing to the field at a particular receiver position and $p_j(r,z)$ is the pressure due to that eigenray. The number of contributing eigenrays can vary considerably, especially at longer ranges.

Once we have associated a phase and intensity with the ray paths we can complete the calculation of the pressure field. As discussed in Chapter 3, equation (3.5), transmission loss (which should be called *coherent transmission loss*) is defined as:

$$\mathrm{TL} \;=\; -20\log\left(\frac{|p(r,z)|}{|p_0|}\right) \qquad \text{dB re 1 m}, \tag{4.23}$$

where p_0 is the pressure for a point source in free space to be evaluated at a distance of 1 m from the source.

Ray methods are most commonly used for high-frequency problems: they are derived under that assumption, where other methods become less practical at higher frequencies. As we go towards high frequencies, the details of the interference pattern are less stable and meaningful. If we consider an acoustic modem operating in the 10-15 kHz band, the interference pattern will vary widely across the band. It will also be very sensitive to details of the sound speed profile that are not measurable.

Under these assumptions, an incoherent calculation may be acceptable in which the phase of the pressure associated with each eigenray is ignored. This leads to:

$$p^{(I)}(r,z) \;=\; \left[\sum_{j=1}^{N(r,z)} |p_j(r,z)|^2\right]^{1/2}. \tag{4.24}$$

Putting equation (4.24) in equation (4.23) we get a TL averaged across all frequencies, which is usually called *incoherent transmission loss*. The incoherent TL option attempts to capture less of the detail of the acoustic field saving on the run time (since phase terms do not enter into calculations), and the incoherent results are much smoother than the coherent ones.

4.1.3 Ray Theory Artifacts

The ray approach as described so far solves the wave equation by introducing a new curvilinear coordinate system formed by the rays. Thanks to this coordinate system one can easily construct travel times and amplitudes by simply solving a set

of ordinary differential equations along each ray. The travel times and amplitudes, of course, yield immediately the pressure field along each ray. However, the user of a ray model typically needs the field on a rectangular grid whose nodes will generally lie between the curvilinear grid formed by the fan of rays.

One simple way to interpolate from the ray grid onto the receiver grid is to construct a beam around each ray. There are two variants: *geometric beam tracing* and *gaussian beam tracing*. Geometric beam tracing produces a piecewise linear interpolation of the pressure field between rays, where the behavior of the beams is determined by the geometry of the ray field. When properly implemented, this approach reproduces precisely a ray theoretic result; however, small errors in the implementation may cause large problems because the beams produced must have precisely the right width to fill the space between adjacent beams. The use of gaussian beam tracing, instead, results in a smoothing of the pressure field.

There are also a few flaws in the transmission loss calculation which are typical of ray-theory results. The first is the occurrence of *shadow zones* where no rays pass and therefore the pressure field is identically zero. The second is the occurrence of *caustics*, which are curves where the cross-section of a ray tube vanishes and therefore the predicted intensity is infinite. The exact solution of the wave equation generally is finite, so this is a ray artifact. In practice, these curves of infinite intensity would normally be missed unless a receiver is placed precisely on a caustic. Nevertheless, the problem can be significant, because the intensity is high not just at the caustic but in a zone surrounding the caustic. Furthermore, there is a phase change that occurs when a ray passes through a caustic. Neglecting this phase change causes an error at subsequent ranges which can be arbitrarily far from the caustic. There are several approaches to produce improved approximations to the field in the vicinity of a caustic; also, caustics are classified into a taxonomy with a finite number of forms (e.g. cusps, swallow-tails,...).

Another ray-theory artifact is explained in Appendix A. For a complete discussion on ray-theory artifacts, including mathematical treatment and clear examples, see [14, pagg. 175-185].

4.2 Available Software

A consistent number of underwater acoustic propagation modeling programs have been placed in the public domain by their authors [23]. Different programs are required for different situations, but together they can perform the majority of common modeling tasks. All these programs are input file driven, and generate output data in a number of different formats.

Acoustic Toolbox by Mike Porter[1] is a collection of acoustic models and related software (written in Fortran and Matlab) for studying sound propagation in an ocean waveguide. Actually, the models have been structured to be suitable for general wave propagation problems; however, the ocean application is the main focus.

The acoustic models included in the package are:

[1]Freely available here: `http://oalib.hlsresearch.com/Modes/AcousticsToolbox/`.

- BELLHOP: for Gaussian beam tracing and ray tracing.
- BOUNCE: for calculation of reflection coefficients for a stack of layers.
- KRAKEN: for the normal modes approach.
- SCOOTER: spectral integral code (also known as wavenumber integration).
- SPARC: a spectral integral code that operates directly in the time domain.

A brief description of BELLHOP, together with the GUI-wrapper AcTUP, is the scope of this section.

4.2.1 BELLHOP

BELLHOP is a beam tracing model for predicting acoustic pressure fields in ocean environments. It is implemented in Fortran, Matlab and Python and is used on multiple platforms (Mac, Windows and Linux).

Various input files must be provided to describe the environment and the geometry of sources and receivers. In the simplest case, which is also typical, there is only one such file: it is referred to as the *environmental file* (it has the .env extension) and includes the sound speed profile, as well as information about the ocean bottom. It allows for range-dependence in the top and bottom boundaries (altimetry and bathymetry), as well as in the sound speed profile. Top and bottom reflection coefficients may also be provided.

BELLHOP produces different output files depending on the options selected within the main environmental file. The main ones are rays, transmission loss and arrivals:

- The ray tracing option produces a file (.ray extension) containing a fan of ray emanating from the source. If the eigenray option is selected, then the fan is winnowed to include only the rays that bracket a specified receiver location. Ray files are usually produced to get a sense of how energy is propagating in the channel.
- If the user is interested in calculating the transmission loss for a tonal source, BELLHOP allows it. After the simulation is finished, the transmission loss information is written to a shade file (.shd extension) which can be displayed as a 2D surface (range-depth plane, intensity as a colormap), or in range and depth slices.
- If one wants to get not just the intensity due to a tonal source, but the entire timeseries then he/she must selects an arrivals calculation. The resulting arrivals file (.arr extension) contains amplitude-delay pairs defining the loudness and delay time for every echo in the channel. This information can be passed to a convolver, which sums up the echoes of a particular source timeseries to produce a receiver timeseries.

Plot programs are provided to display each of the input and output files' content. See [21, 24] for a detailed description of BELLHOP features, including lots of examples of input and output files.

4.2.2 AcTUP

AcTUP V2.2*l*[2] is a GUI-wrapper for Mike Porter's Acoustic Toolbox developed by Alec J. Duncan and Amos L. Maggi that provides a simple, consistent interface for running its various propagation routines. The GUI is written in Matlab, and provides a variety of input and output data visualization tools [25]. See [22] for the full list of codes supported by AcTUP V2.2*l*.

All the simulations and results described in the next chapter were obtained using the BELLHOP version included in AcTUP V2.2*l*; although quite old (the latest release is from 2006) it still proved itself useful for the scopes required. Appendix D illustrates a quick start guide to set up a simple simulation with this toolbox.

[2]Freely available here: `http://cmst.curtin.edu.au/products/actoolbox.cfm`.

Chapter 5

Acoustic Channel Simulations

This chapter illustrates the application of BELLHOP ray tracing model to the simulation of marine environmental conditions during CommsNet13 sea trials. These simulations were done in order to characterize the acoustic propagation and therefore to predict possible losses and transmission failures between the USBL-vehicle and the acoustic modems on the sea bottom. Both morning and afternoon CTD-measured sound speed profiles were included, and the results were compared with a standard isospeed profile (i.e. constant with depth, typical of shallow waters in the winter period) in the same conditions.

Section 5.1 describes in detail the methods and the simulation parameters. These include environmental parameters (e.g. source and receiver depths), and the parameters needed by BELLHOP to run the simulations, which represent the typical features of ray tracing models introduced in Section 4.1.

Section 5.2 is where the results obtained with these simulations are presented and discussed. They are: ray plots, which give an idea about how energy propagates through the channel; transmission loss (signals attenuation), which is showed both in 2-D range-depth plots and 1-D slices for a fixed receiver depth; and amplitude-delay arrivals (eigenrays), i.e. the rays that connect a specific source-receiver pair and allow to calculate the impulse response of the acoustic channel.

5.1 Methods and Parameters

As stated at the end of the previous chapter, the BELLHOP version used in this work is the one included in the GUI-wrapper AcTUP v2.2*l*. Table 5.1 lists the most important simulation parameters. As we can see, receiver and source depths were inverted: this didn't change the final result, thanks to the acoustic reciprocity

	Frequency (kHz)	Bottom Depth (m)	Source Depth (m)	Receiver Depth (m)
Morning	30	30	29	0.5
Afternoon				5.5

Table 5.1: Simulation and environmental parameters.

Type	ρ (Kg/m^3)	c_p (m/s)	c_s (m/s)	α_p (dB/λ_p)	α_s (dB/λ_s)
Silt/Sand	1700	1613	225	0.9	2

Table 5.2: Sea bottom geoacoustic properties.

principle (see Section 3.3.3), and allowed for a simpler interpretation of the results. In fact, what changes its position with time is the USBL-vehicle on the surface, not the modem on the bottom. The extra 0.5 m of depth were added to account for the position of the USBL-modem, which was mounted on the vehicle's hull.

The ocean surface was modeled as a vacuum, while the bottom geoacoustic parameters (listed in table 5.2) were those of a mixed silt/sand type; see table 3.1 for comparisons. The water column was completely characterized by the sound speed profiles depicted in figure 2.6, together with the standard density of 1024 Kg/m^3 (i.e. no range-dependent environment). The value chosen for the isospeed profiles was the first one taken from real data, i.e. the sound speed measured right beneath the sea surface.

As for the receiver locations[1], a uniform spatial distribution was chosen with a resolution of 0.5 m in depth and 1 m in range, which was fine for the problem considered. All the results displayed in the following sections were obtained with the gaussian beam option selected (see Section 4.1.3), since this produced more accurate and smooth TL and arrivals plots, at the price of a slightly increased computation time.

5.2 Simulation Results

5.2.1 Ray Plots

Figure 5.1 shows the ray plots for all the environmental conditions simulated with BELLHOP. The number of traced beams was 40 (with an angular limit of $\pm 85°$), otherwise the plots would become too cluttered. The convention followed is that the angles are specified in declination, i.e. zero degrees is a horizontally launched ray, and a positive angle is a ray launched toward the bottom.

The main thing to notice is the difference of ray patterns between isospeed and real sound speed profiles near the sea bottom. The result is very similar to the paths depicted in figure 3.5, and it is certainly due to the strong negative gradient of measured SSP (visible in figure 2.6), as a consequence of Snell's Law: basically, all the rays are attracted to the region where sound speed reaches its minimum value, and change their path to get towards it. No particular differences were found instead between morning and afternoon conditions, since the profiles were very similar.

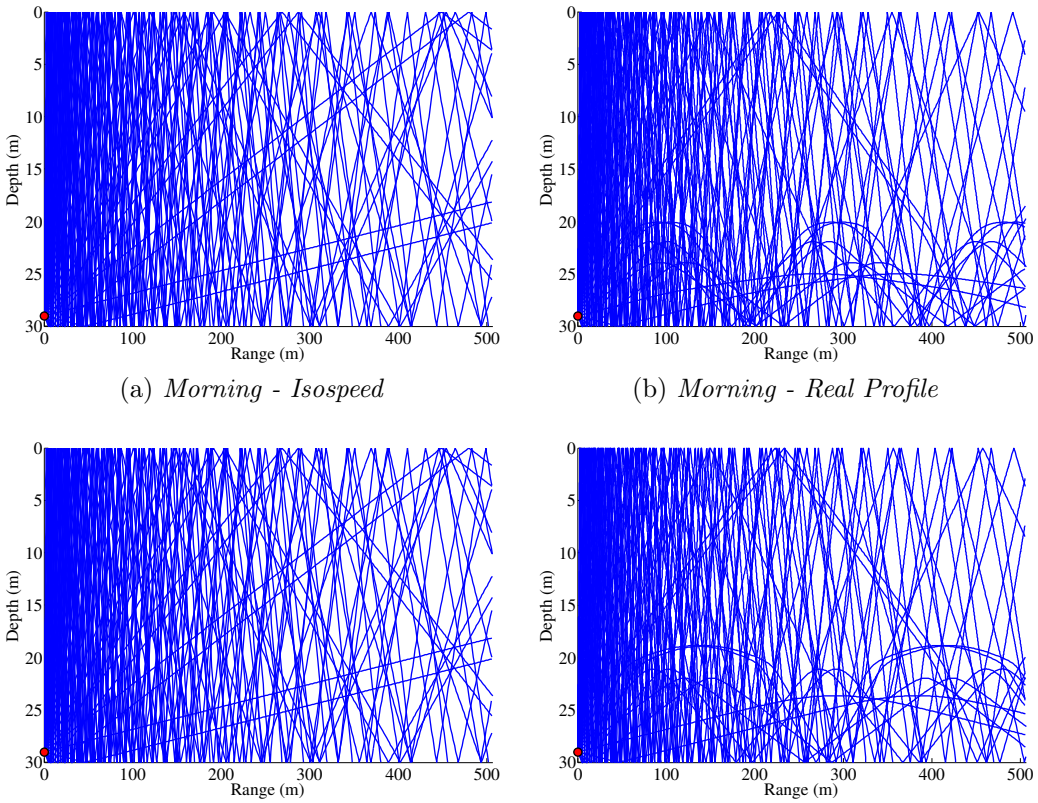

(a) *Morning - Isospeed* (b) *Morning - Real Profile*

(c) *Afternoon - Isospeed* (d) *Afternoon - Real Profile*

Figure 5.1: Ray plots for morning and afternoon environmental conditions.

5.2.2 Transmission Loss

Figure 5.2 displays the incoherent transmission loss plots obtained with BELLHOP for all the simulated environmental conditions. We decided to show the incoherent and not the coherent TL since the former is much smoother and clearly points out the differences between the various conditions. As we can see, these plots are in accordance with figure 5.1, i.e. the transmission loss clearly follows the ray paths. This is particularly evident for the measured SSP plots (right), since transmission loss for shallow waters with a constant speed of sound (left) follows the cylindrical spreading rule (see Section 3.1.2) and gives much less information. The region where rays behavior becomes different from the isospeed case starts at about 22 m in depth and 100 m in range (distance from the source), and this convergence produces a lower TL value near the bottom, where the rays are less dispersed. As a consequence, in order to keep the energy balance, one would expect the TL to become higher at low depths.

This is confirmed in figures 5.4 to 5.6. At higher depths (25 m), near the bottom, ray paths in the real case produce a gain of almost 4 dB both for afternoon and morning situations, while at low depths (0.5 and 5.5 m) the TL is 1-2 dB higher than the isospeed case as expected. Table 5.3 lists these differences for all these

[1]We refer to the "virtual" receveirs, i.e. those needed by BELLHOP to calculate and display the acoustic field.

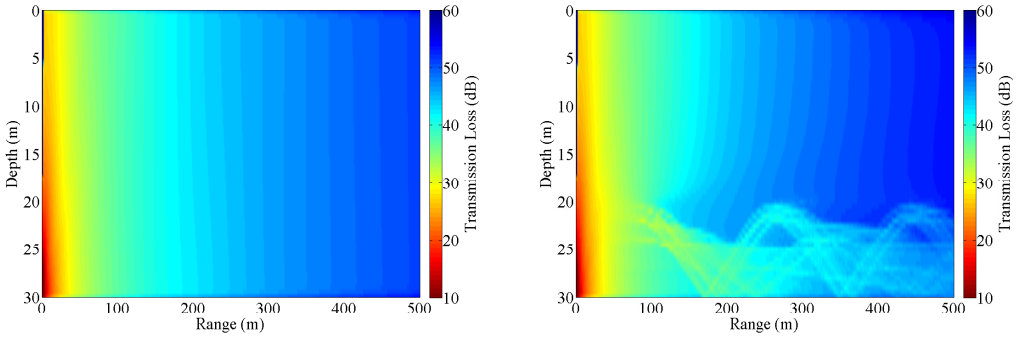

(a) *Morning - Isospeed*

(b) *Morning - Real Profile*

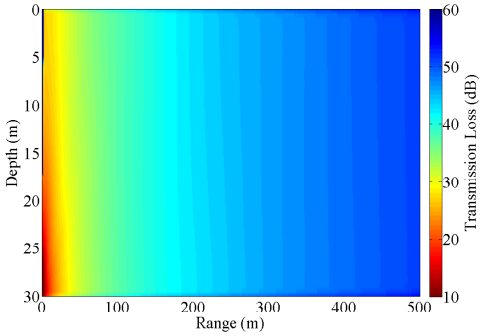

(c) *Afternoon - Isospeed*

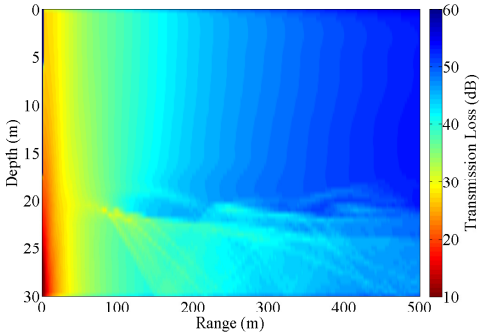

(d) *Afternoon - Real Profile*

Figure 5.2: Incoherent TL plots for morning and afternoon environmental conditions.

cases: positive values show a higher TL for the real case, while negative ones a lower TL (i.e. lower signal attenuation). We chose these values for the receiver ranges (horizontal distances from the source) since they were the typical ranges of operation of the Typhoon vehicle during the CommsNet13 experiment.

Finally, no significant variations were found between morning and afternoon environmental conditions for real SSP simulations, see figure 5.3.

5.2.3 Arrivals

A very interesting and useful feature of BELLHOP is the creation of a file that contains all the arrivals (i.e. rays, parametrized by complex amplitude and phase) from the source for each specified receiver in the environment, together with their delay time. This is equivalent to construct the transfer function of the acoustic channel, and allows to better analyze signal transmission from source to receiver (which is what we did in Chapter 6).

To better capture and interpret the importance of these arrivals, we examine once again three different receiver positions, in range: 200 m, 300 m and 400 m. Receivers depths were 0.5 m for morning and 5.5 m for afternoon (where the Typhoon always stayed under the sea surface).

Figures 5.7 to 5.9 show the arrivals sequences as stem plots for morning experimental conditions, comparing isospeed and real sound speed profile. Since ray

Receiver Depth	Environmental Conditions	Receiver Range		
		200 m	300 m	400 m
0.5 m	Morning	1.17	2.08	2.79
	Afternoon	0.97	1.68	2.32
5.5 m	Morning	1.08	1.67	2.16
	Afternoon	0.99	1.48	1.93
25 m	Morning	-3.71	-3.84	-3.89
	Afternoon	-2.91	-3.87	-4.07

Table 5.3: Incoherent TL difference from ideal to real case.

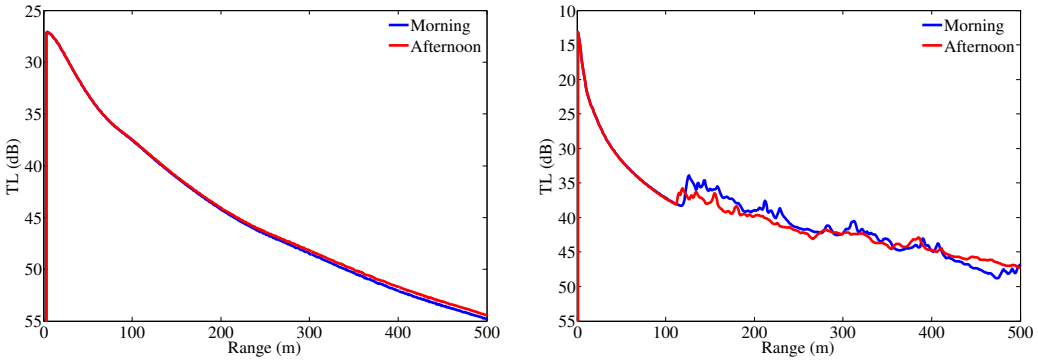

(a) *Depth 0.5 m* (b) *Depth 25 m*

Figure 5.3: Morning and afternoon incoherent TL slices for real sound speed profile.

amplitude is a complex number (to account for phase changes and caustics), the quantity on the y-axis is its modulus. As one would expect, replicas of source signal increase with range, due to reflections and multipath effects; the same happens for the arrival times (greater distance to cover) and amplitude values, which decrease due to geometrical spreading (at least). Another thing to point out is the higher number of arrivals when the sound speed profile is the real one, which means that signal transmission encounters much more interference in this case.

Figures 5.10 to 5.12 do the same for afternoon simulations, and the same exact considerations can be made. It is worth noticing that, probably due to the higher receiver's depth, the arrivals number is higher too (with respect to morning conditions).

As previously stated, the importance of these data lies in the fact that they can be convolved with the signal coming from source in order to obtain the signal that reaches the receiver; this allows for an in-depth analysis of the transmission conditions of the acoustic channel, which is the subject of the following chapter of this document.

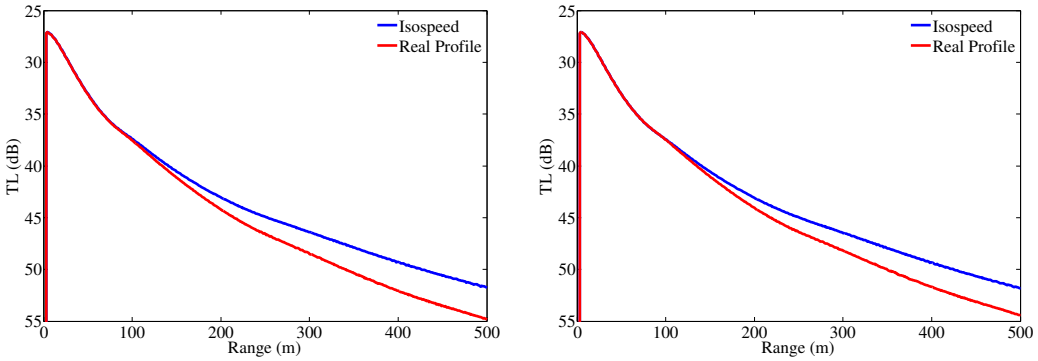

(a) *Morning* (b) *Afternoon*

Figure 5.4: Incoherent TL slice for isospeed and real profile simulations, receiver depth 0.5 m.

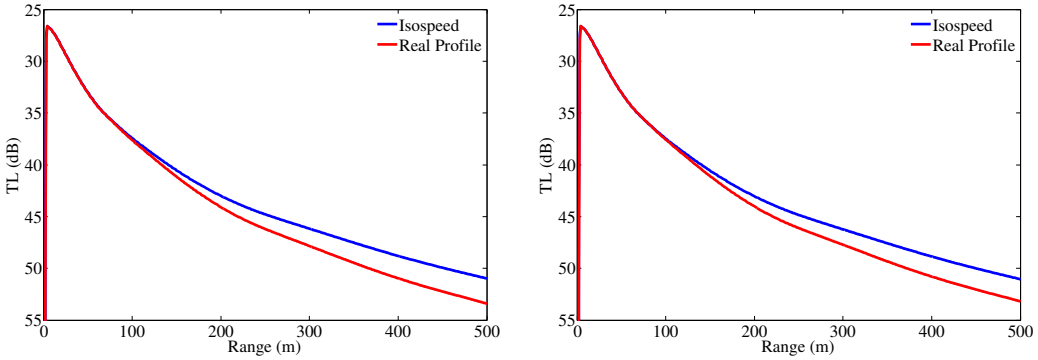

(a) *Morning* (b) *Afternoon*

Figure 5.5: Incoherent TL slice for isospeed and real profile simulations, receiver depth 5.5 m.

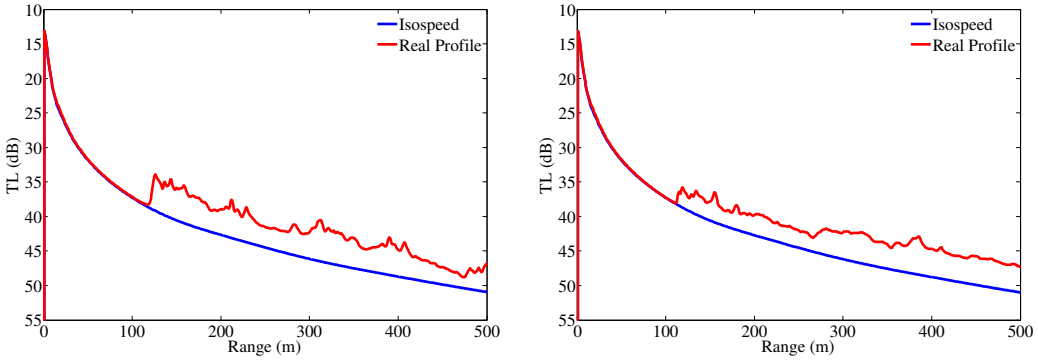

(a) *Morning* (b) *Afternoon*

Figure 5.6: Incoherent TL slice for isospeed and real profile simulations, receiver depth 25 m.

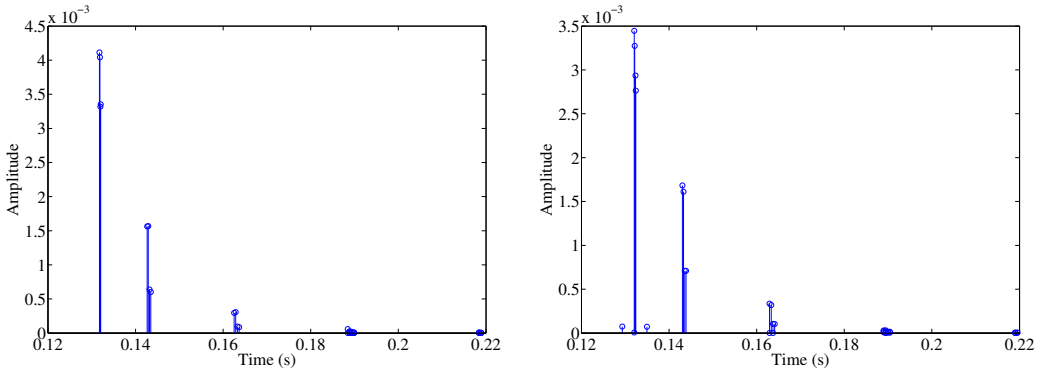

(a) *Isospeed* (b) *Real Profile*

Figure 5.7: Arrivals for receiver range 200 m, morning conditions.

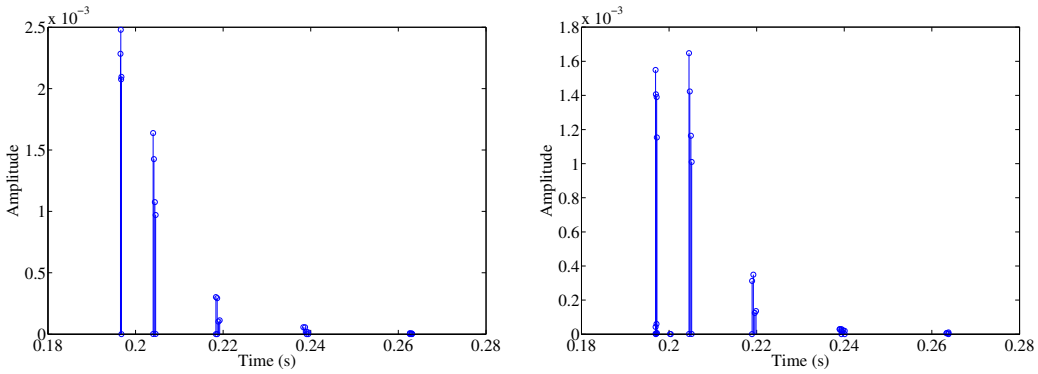

(a) *Isospeed* (b) *Real Profile*

Figure 5.8: Arrivals for receiver range 300 m, morning conditions.

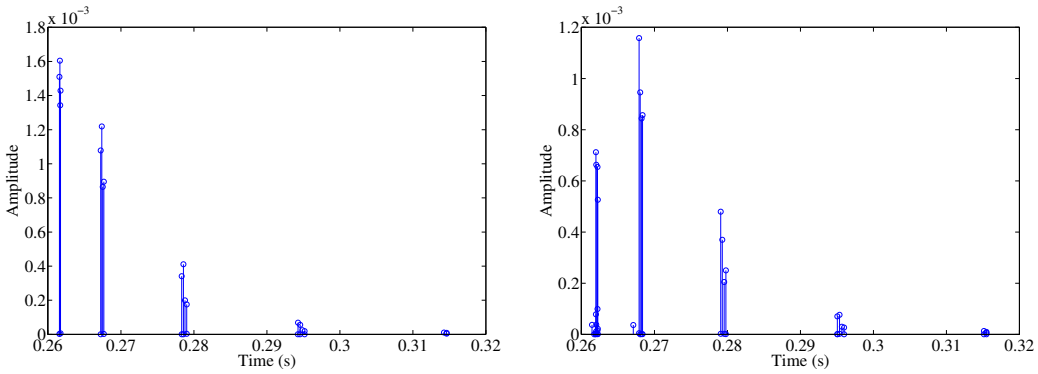

(a) *Isospeed* (b) *Real Profile*

Figure 5.9: Arrivals for receiver range 400 m, morning conditions.

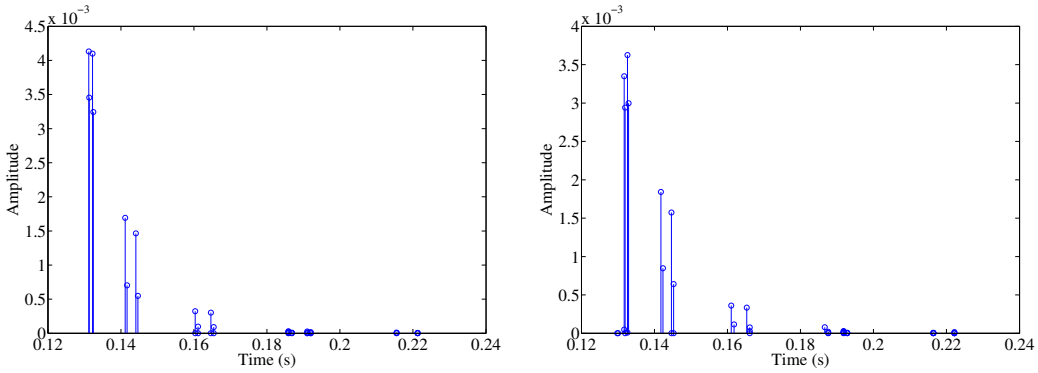

(a) *Isospeed* (b) *Real Profile*

Figure 5.10: Arrivals for receiver range 200 m, afternoon conditions.

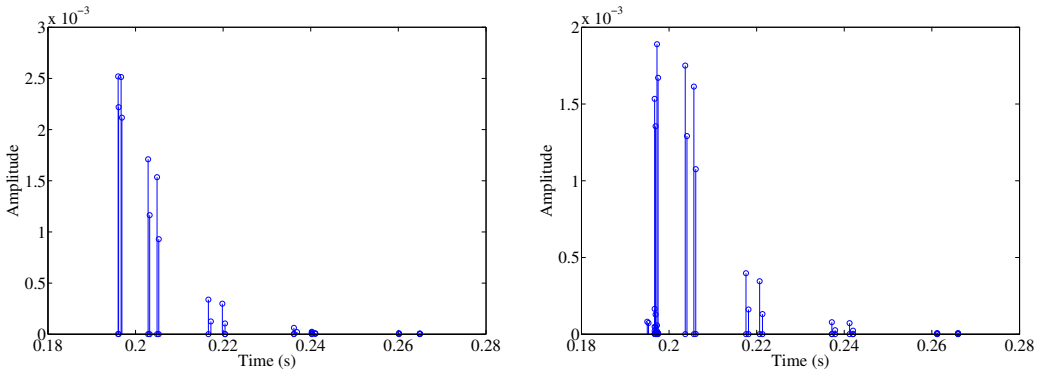

(a) *Isospeed* (b) *Real Profile*

Figure 5.11: Arrivals for receiver range 300 m, afternoon conditions.

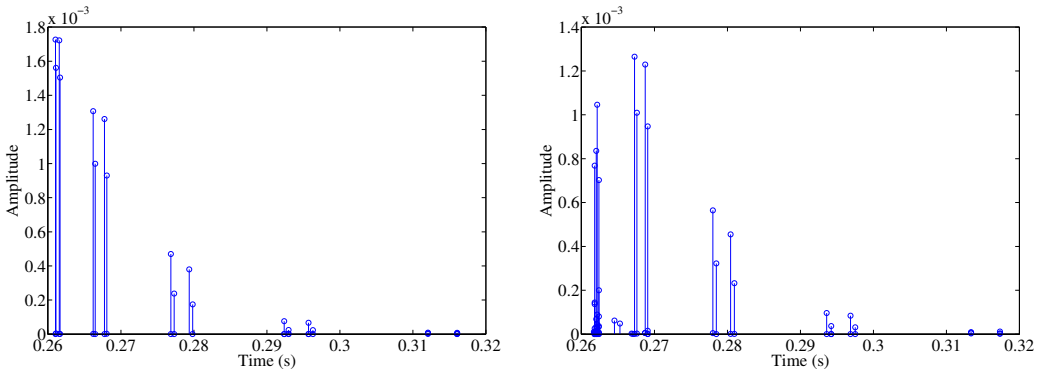

(a) *Isospeed* (b) *Real Profile*

Figure 5.12: Arrivals for receiver range 400 m, afternoon conditions.

Chapter 6

Transmission Quality Analysis

In Chapter 5, BELLHOP was used to completely characterize the underwater acoustic channel from CommsNet13 measured sound speed profiles, both for morning and afternoon environmental conditions. The next step is to use the obtained data to analyze the transmission quality from source (the acoustic modem) to receiver (the USBL-vehicle), which can be subjected to interference and multipath effects, in order to explain possible communication failures and therefore to better design the geometry of communication for future experiments. This chapter describes and discusses in detail all the results obtained with this analysis.

The starting point were the arrivals files generated with BELLHOP for each simulation; as we previously stated, these files contain the amplitude-delay pairs of the propagated rays for each receiver, which can be used to construct the impulse response of the channel. Therefore, they played a central role in the received signals calculation and in the following developments.

Section 6.2 contains the transmission quality analysis using the classical cross-correlation approach. We performed a simple cross-correlation calculation between source signal (input) and received signal (output) in order to test the correctness of the transmission. If the signal is transmitted through the channel without interference, we would see a delayed peak in the cross-correlation function, with the delay due to the distance between source and receiver. If we set an appropriate threshold, the receiver can correctly detect the signal reception when the peak is above this value.

Section 6.3 describes the transmission quality analysis using source signal reconstruction in the case of fixed geometry of communication (no source-receiver relative motion). Assuming that the receiver knows the basic waveform the source implements to send signals with, it can use this information together with the received signal in order to perform a reconstruction of the real (unknown) source signal in two steps: first, estimate the impulse response of the system (the acoustic channel), then deconvolute the received signal through this impulse response to obtain an estimate of the source signal. The cross-correlation analysis between this estimated source signal and an exact replica of the basic source signal can yield much better results for signal detection.

Section 6.4 repeats the steps described in the previous section for the case of variable geometry of communication (there is a source-receiver relative motion), which was the real situation encountered during the CommsNet13 experiment. If

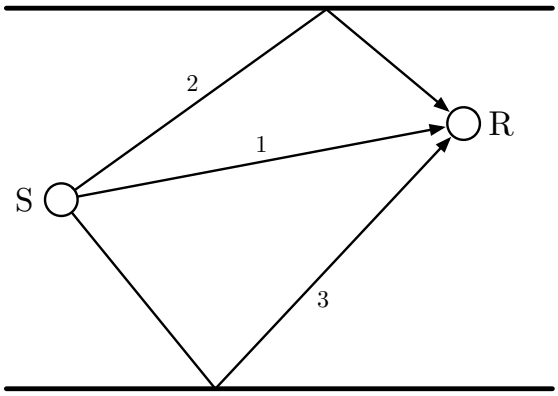

Figure 6.1: A simple example of a source-receiver configuration in a waveguide.

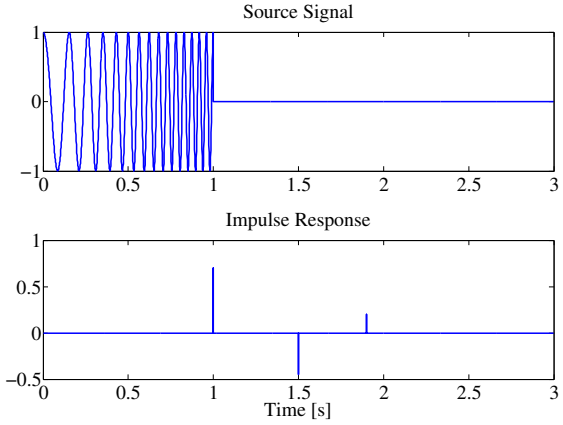

Figure 6.2: Source signal and channel impulse response example.

this happens, the received waveform is influenced by the Doppler shifts determined by the relative motion, which must be taken into account when signal detection is performed.

The mathematical tools used to produce all the results presented in this chapter are described in the appendices. Received signal calculation (Appendix A) makes use of the Hilbert transform of the source signal, since rays are described by complex pressure to accounts for phase changes and caustics. Then Appendices B and C explain the methods, correlation analysis and deconvolution via regularized least squares, which were used to eliminate multipath effects and to test whether the receiver can obtain an accurate reconstruction of the real transmitted signal.

6.1 Source Signal and Cross-Correlation

Figure 6.1 illustrates a simple example of a waveguide where a source (S) emits three acoustic rays which arrive at a receiver (R) in three different ways: the first one directly, the second one reflected by the sea surface and the third one reflected by the sea bottom. Each of these rays (arrivals) constitute a replica of the original signal, and their summation at the receiver creates interference.

To better illustrate this fact we can see figures 6.2 and 6.3. We suppose that

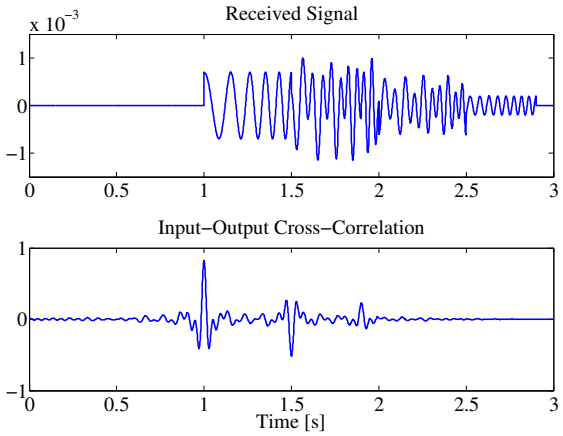

Figure 6.3: Received signal and cross-correlation for the previous example.

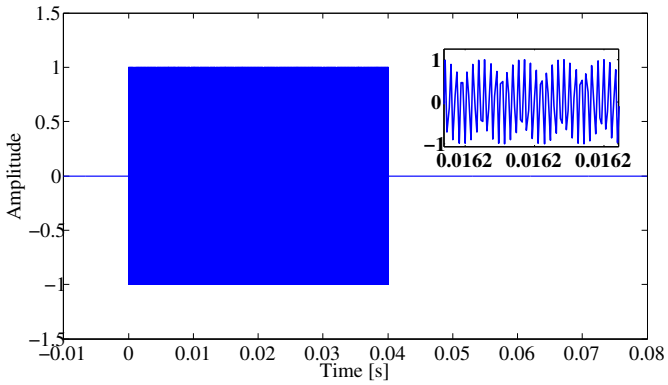

Figure 6.4: Source signal (sweeping sinusoid), with an enlargement.

the impulse response of the channel is known and has the structure represented in figure 6.2. If we make the convolution between this impulse response and the source signal, we get the received signal shown in figure 6.3; in order to see what happened to the original one, we can calculate the cross-correlation between input and output using equation (B.4), and the correlation function clearly highlights the presence of the three signal replicas over time.

The same analysis was done for signal transmission between source and receiver during CommsNet13 sea trials. Now, the impulse response is available thanks to the arrivals files produced by BELLHOP. The waveform used as the source signal was a chirp (sweeping sinusoid), which is implemented on the EvoLogics acoustic modem mounted on the USBL-vehicle. The lowest frequency was 18 kHz, while the highest was 34 kHz. The chirp duration was 40 ms, while the total time window of observation was 80 ms. The signal is shown in figure 6.4, with an enlargement to point out its structure. It is well-known that chirps properties produce an auto-correlation equal to a sinc function with the peak perfectly centered in the origin of the time axis, as we can see from figure 6.5.

As for the received signal visualization, the time scale was chosen as the *reduced time* (see [14, pagg. 615-616]), which represents a relative time that takes into

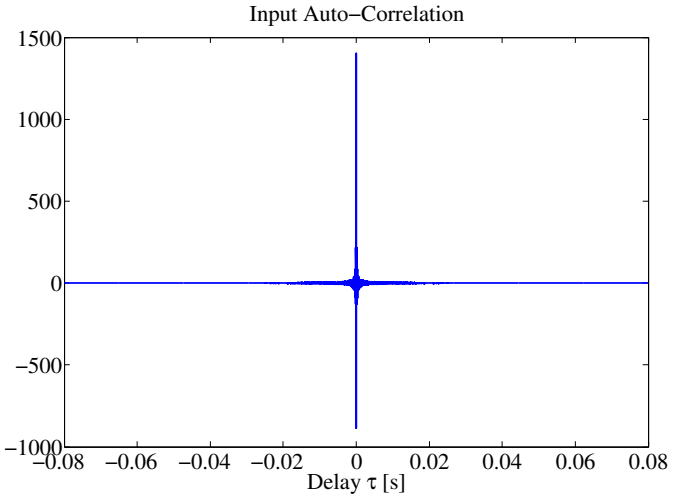

Figure 6.5: Source signal auto-correlation function.

account the distance between source and receiver. It is usually calculated as:

$$t_{red} = t - \frac{r}{c_{red}}, \tag{6.1}$$

where t is the absolute time, r is the receiver range and c_{red} is the reduced speed of sound, which should always exceed the fastest possible arrival. For our purposes, we chose $c_{red} = 1700\text{m/s}$.

We previously stated that typical horizontal vehicle distances from the source (ranges) were 200 m, 300 m and 400 m. Hereinafter, for the sake of space, all the results will be shown only for range equal to 200 m (both during morning and afternoon), since results for the other two cases were very similar. We also need to point out that this whole analysis was made in the case of exact knowledge of all signals (deterministic case), without the influence of noise or other sources of error (stochastic case).

6.2 Signal Detection with Classic Correlation

Figure 6.6 display the received signals calculated for morning and afternoon environmental conditions when the receiver range is equal to 200 m. Figure 6.7 does the same for their cross-correlation functions with the original source signal.

It becomes immediately clear that the original signal reaches the receiver heavily distorted and attenuated due to the interference and multipath reflections of the acoustic channel. Cross-correlation shapes clearly reflect the arrivals depicted in figure 5.7 (for morning) and figure 5.10 (for afternoon), and the attenuation becomes greater as range increases.

It is impossible for the receiver to correctly detect the signal, since *a)* there is a tremendous loss between auto-correlation and cross-correlation values (the former reaches a peak of almost 1500, the latter between 2 and 6), and *b)* the ratios between the first and the second peak in cross-correlation functions are too small, which means that, even if we set an appropriate threshold on the cross-correlation

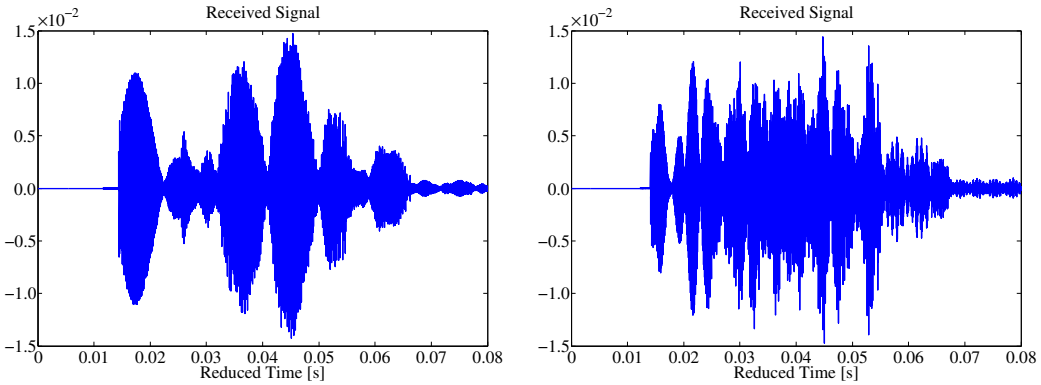

(a) *Morning* (b) *Afternoon*

Figure 6.6: Received signals for morning and afternoon conditions, range 200 m.

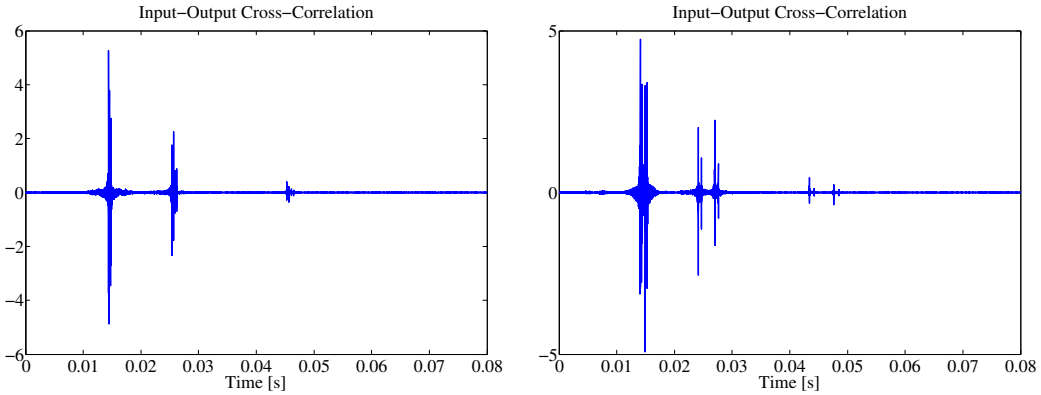

(a) *Morning* (b) *Afternoon*

Figure 6.7: Cross-correlation functions for morning and afternoon conditions, range 200 m.

for signal detection, the receiver becomes too sensible to fluctuations of the signal (noise, outliers, ...).

6.3 Signal Detection with Source Estimation

6.3.1 Impulse Response Estimation

The first step in source signal estimation was to use the received signal and an exact replica of the basic source waveform to obtain an estimate of the impulse response of the channel. As previously mentioned, the procedure (correlation analysis) is described in Appendix B and the results are shown in figure 6.8. The number M of samples used during this process was exactly the half of the original signals.

If we make a comparison with the cross-correlation functions shown in figure 6.7 we see that the impulse response estimate is very reliable (they both give information on signal replicas over time) and similar to the original one; the only difference is the absence of the last part due to the reduced number of samples, but this values

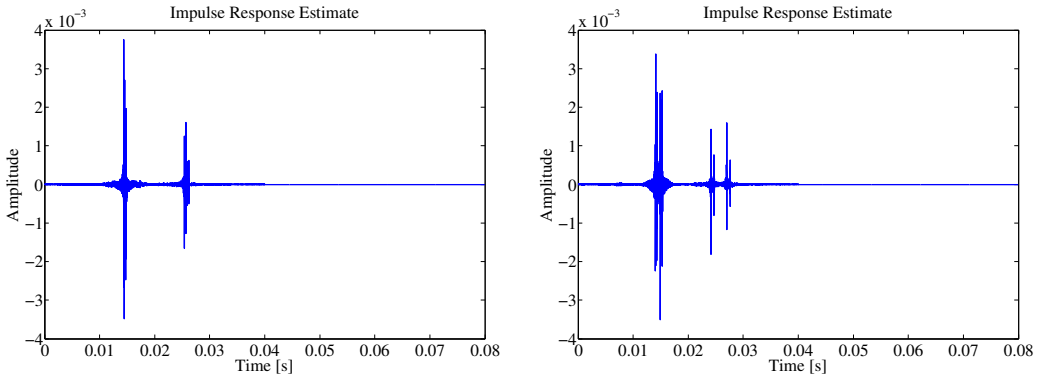

(a) *Morning* (b) *Afternoon*

Figure 6.8: Impulse response estimates for morning and afternoon conditions, range 200 m.

are very small and have non influence on signal estimation.

6.3.2 Source Signal Estimation

Then, the estimated impulse response and the received signal can be used to perform a deconvolution to obtain the source signal. The receiver can perform a cross-correlation between this one and the true waveform in order to ensure the correct signal detection. Since the values of all the vectors are very small the problem is bad-conditioned, so we were forced to use a modified deconvolution algorithm which introduces a *regularization parameter* λ (as described in Appendix C); the results of the deconvolution are therefore influenced by the values of this scalar parameter.

Figures 6.9 and 6.10 show the results of this process for two values of λ. In the first case, the regularization parameter is high (compared to the order of magnitude of signal values), and this produces an estimate of the source signal which is too similar to the received signal[1]. Even though the cross-correlation between them has a single peak centered at the origin of the time axis (which is what we want), the value of this peak is still too small because of received signal attenuation due to channel effects.

The second case is the opposite: the regularization parameter value is now very small, and this does not solve the deconvolution numerical problems, that are clearly visible in the left part of figure 6.10. Cross-correlation has now a bigger peak at the beginning, but the presence of oscillations in the right part is undesired, since we want this function to be the most similar possible to a standard chirp auto-correlation function (figure 6.5).

6.3.3 Regularization Parameter Sensitivity

We then performed a sensitivity analysis of the estimate based on this parameter. We calculated the source signal estimate for every value of λ on an equally

[1]This means that the λI term in equation (C.4) dominates.

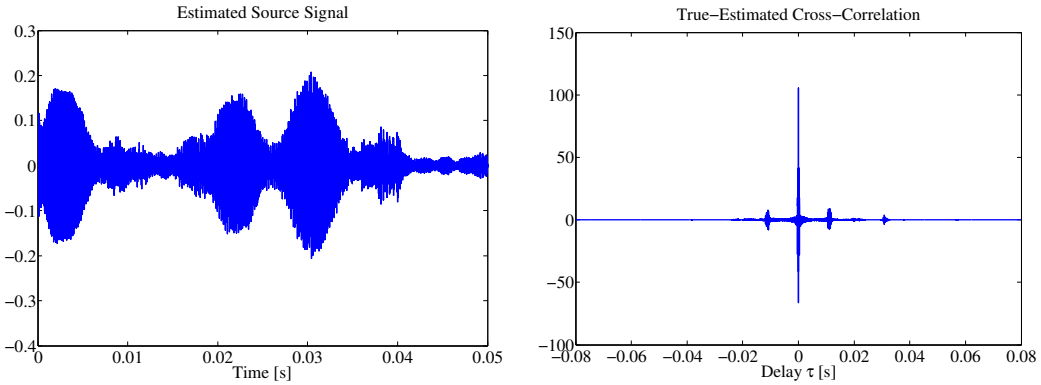

(a) *Estimated Signal* (b) *Cross-correlation*

Figure 6.9: Estimated source signal and cross-correlation function for morning conditions, range 200 m, when $\lambda = 10^{-3}$.

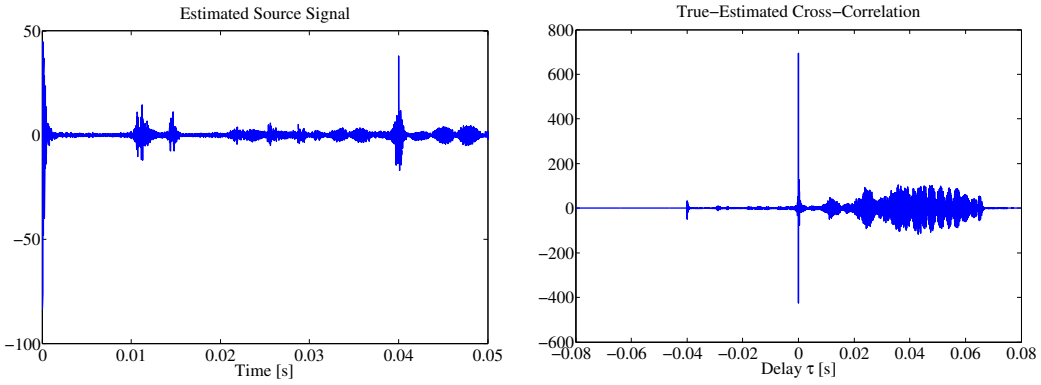

(a) *Estimated Signal* (b) *Cross-correlation*

Figure 6.10: Estimated source signal and cross-correlation function for morning conditions, range 200 m, when $\lambda = 10^{-10}$.

logarithmic-spaced grid between 10^{-12} and 1. Figure 6.11 plots the so called *cross-correlation penalty* against the $\log_{10}$ values of the regularization parameter. The cross-correlation penalty p_{corr} was calculated in this way:

$$p_{corr} = \frac{P}{\sum_i p_i^{th}}, \tag{6.2}$$

where P is the cross-correlation peak (between the estimated and the true signals) and p_i^{th} are all the other values of cross-correlation function that exceed a predefined percentage of the peak value. For every case, this percentage was chosen as 5%, which is very precautionary.

The "optimal" value of λ for deconvolution was chosen as the one which maximizes the penalty p_{corr}. This was done in order to obtain the estimate which has the most similar cross-correlation function to that of a chirp signal (peak at the beginning, very small values elsewhere). For example, in the morning-200 m range case, the optimal regularization parameter λ_{opt} is equal to $8.85 \cdot 10^{-6}$, and

Environment	**Range**	**Peak**	$\boldsymbol{\lambda_{opt}}$
Morning	200 m	555.61	$8.85 \cdot 10^{-6}$
	300 m	586.47	$2.07 \cdot 10^{-6}$
	400 m	638.94	$1.13 \cdot 10^{-7}$
Afternoon	200 m	676.54	$2.63 \cdot 10^{-8}$
	300 m	671.96	$6.16 \cdot 10^{-9}$
	400 m	576.17	$2.07 \cdot 10^{-6}$

Table 6.1: Cross-correlation peaks and λ_{opt} for conditions of interest.

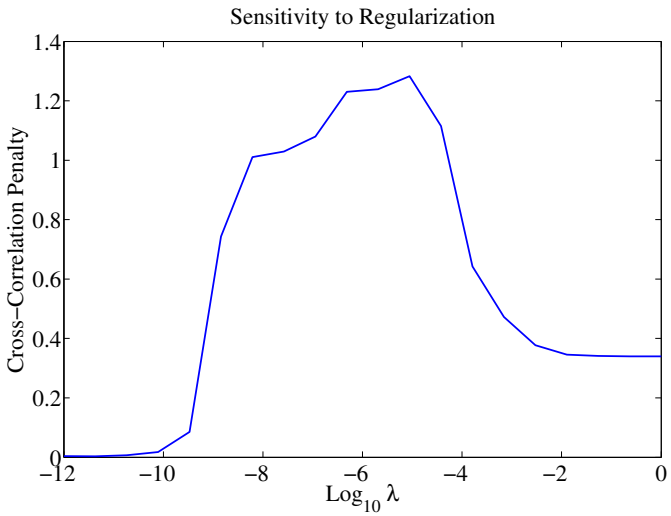

Figure 6.11: Sensitivity analysis to regularization parameter for morning conditions, range 200 m.

it produces a cross-correlation peak of 555.61; the estimated source signal and the cross-correlation function are visible in figure 6.12.

Table 6.1 lists the results of this procedure for every condition of interest. The conclusions are quite straightforward: if the receiver implements even a simple reconstruction procedure as the one described in this section, it can get rid of the interference and multipath effects of the acoustic channel, obtain a good estimate of the true source signal and, setting up an appropriate threshold for the cross-correlation peak value, correctly detect its transmission. In practice, acoustic modems and transponders implement even more refined reception algorithms.

6.4 Signal Detection with Doppler Shift

The results showed in the previous sections are valid for the case of stationary source-receiver configuration. Since the receiver (the USBL-vehicle) was moving during the experiment, the frequency shifts due to Doppler effects must be taken into account during received signal calculations, as explained in the last part of Appendix A.

The magnitude of the Doppler effect is proportional to the ratio $a = v/c$ of the

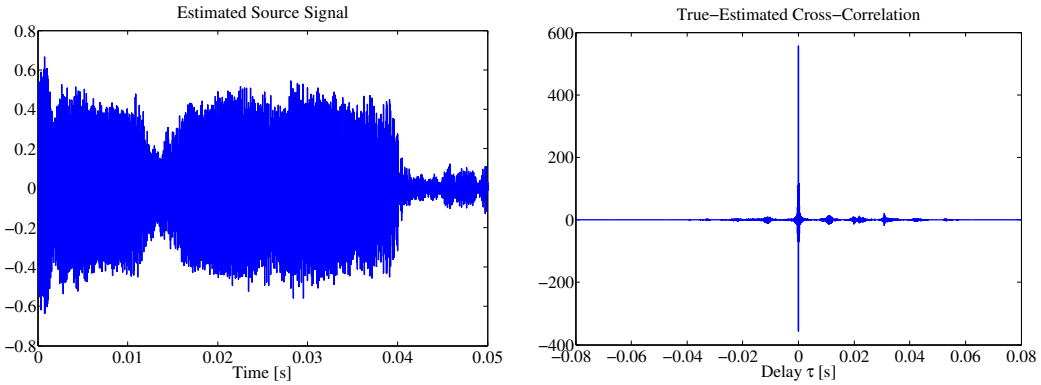

(a) *Estimated Signal* (b) *Cross-correlation*

Figure 6.12: Estimated source signal and cross-correlation function for morning conditions, range 200 m, when $\lambda = \lambda_{opt}$.

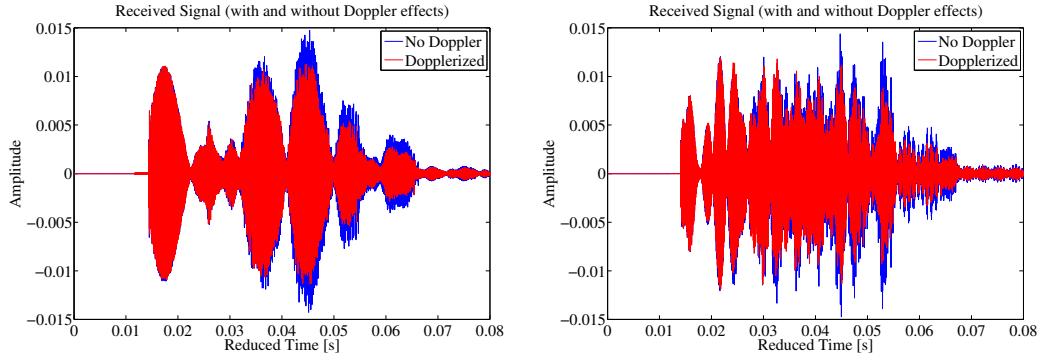

(a) *Morning* (b) *Afternoon*

Figure 6.13: Received signals comparison with and without Doppler effects at range 200 m, receiver speed 1 m/s.

relative transmitter-receiver velocity to the speed of sound. Because the speed of sound is very low compared to the speed of electromagnetic waves, motion-induced Doppler distortion of an acoustic signal can be extreme. For comparison, in the case of a mobile radio system, at 160 km/h we have $a = 1.5 \cdot 10^{-7}$. This value is low enough that Doppler spreading can be neglected. Instead, a stationary acoustic system may experience unintentional motion at 0.5 m/s (1 knot), which would account for $a = 3 \cdot 10^{-4}$. For an AUV moving at several meters per second (submarines can move at much greater velocities), factor a will be on the order of 10^{-3}, a value that cannot be ignored [26].

Figure 6.13 shows the comparison between the received signals calculated with and without Doppler effects, when the horizontal speed of the vehicle is equal to 1 m/s (i.e. 2 knots)[2]. As wee can see, the only substantial difference from the stationary case is a slightly higher attenuation of the signal, while its shape (the resulting envelope produced by the convolution with the arrivals) remains the same. At much higher speeds, for example 10 m/s (see figure 6.14), there is also a time

[2]The typical vehicles speeds during CommnsNet13 trials were 0.5, 1 and 1.5 knots.

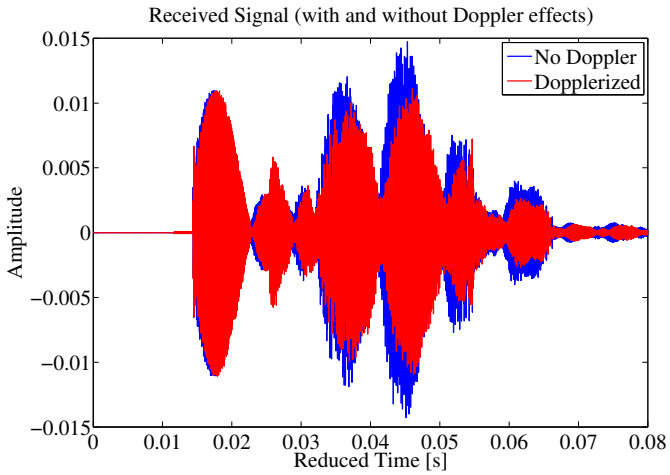

Figure 6.14: Received signals comparison with and without Doppler effects for morning conditions at range 200 m, receiver speed 10 m/s.

shift, which is significant especially at the higher frequencies of the signal (right part), but once again the signal shape remains the same.

We used the dopplerized signals in the reconstruction procedure described in Section 6.3, and results were exactly the same (we do not report them for the sake of brevity). This means that the Doppler shifts do not influence the impulse response of the acoustic channel, and become significant only at very high relative speeds between source and receiver, which fall out the range of interest for our analysis.

Conclusions

Starting with real data of sound speed profiles, and using the ray tracing numerical simulator BELLHOP with the appropriate settings, the acoustic environmental conditions of the La Spezia Gulf during CommsNet13 trials were completely characterized. The differences from a standard isospeed profile, typical of shallow waters during winter, were examined; we saw that the strong negative gradient of measured SSPs near the bottom produces a convergence of the ray paths, which translates in a lower TL at high depths and, to maintain the energy balance, a higher TL at low depths (the ones the USBL-vehicle was operating at).

Then, with the contribution of amplitude-delay arrivals files generated from BELLHOP simulations, an extensive analysis was done of the transmission quality between source (the USBL-vehicle) and receiver (the moored modems) in these conditions. Using a standard chirp waveform as the source signal, we realized that the interference and multipath effects produced by the acoustic channel greatly worsen the signal transmission, and the signal reaches the receiver distorted and poorly correlated with the original one. Therefore, assuming that the receiver knows the basic waveform the source uses to communicate with, it could follow a mathematical procedure to reconstruct the source signal starting from the received one, in two steps: impulse response estimation with correlation analysis and source signal estimation using regularized least squares deconvolution. The results obtained clearly showed that with this procedure the receiver can get rid of all the interference and, after obtaining an estimate of the source signal which is very close to the real one, greatly improve the transmitted signal reception. Both the cases of stationary and non-stationary source-receiver configurations were analyzed.

The contents of this thesis were elaborated in order to try to explain the irregular acoustic position fixes encountered in the localization of the USBL-vehicle during CommsNet13 sea trials. Since we showed that the acoustic channel influences can be eliminated with an appropriate reception algorithm, they could only be explained in two ways:

- The acoustic modems were working at the limit of their detection threshold, which means that the little changes in TL between isospeed and measured profiles (table 5.3) become significant.
- Fluctuations in sound speed values and/or other physical parameters can have some influence and therefore they must be taken into account.

More data must be collected and further analyses and simulations must be done in order to more accurately explain these phenomena.

Appendix A

Received Signal Calculation

This section is based on [14, pagg. 617-619]. Received signal calculation using the formulation of ray theory in the time domain has a particularly simple form. We denote the source signal with $s(t)$. The easiest way of obtaining the desired result is to start with the pressure contribution of a single eigenray (see Section 4.1):

$$p(s) \;=\; A(s)e^{i\omega\tau(s)}, \tag{A.1}$$

where $A(s)$ is the amplitude and $\tau(s)$ is the phase delay along the ray path s:

$$\tau(s) \;=\; \int_0^s \frac{1}{c(s')}\,\mathrm{d}s'. \tag{A.2}$$

We assume that the loss, and therefore the amplitude term $A(s)$, is independent of frequency. A time domain solution can be directly obtained by Fourier synthesis as:

$$p(s,t) \;=\; \frac{1}{2\pi}\int_{-\infty}^{+\infty} S(\omega)p(s,\omega)e^{-i\omega t}\,\mathrm{d}\omega, \tag{A.3}$$

where $S(\omega)$ represents the spectrum of the source. Substituting the ray representation for $p(s,\omega)$, we obtain:

$$p(s,t) \;=\; A(s)\frac{1}{2\pi}\int_{-\infty}^{+\infty} S(\omega)e^{-i\omega[t-\tau(s)]}\,\mathrm{d}\omega, \tag{A.4}$$

that is:

$$p\big[s,t+\tau(s)\big] \;=\; A(s)\frac{1}{2\pi}\int_{-\infty}^{+\infty} S(\omega)e^{-i\omega t}\,\mathrm{d}\omega. \tag{A.5}$$

We can recognize the integral as simply the inverse Fourier transform so that:

$$p\big[s,t+\tau(s)\big] \;=\; A(t)S(t), \tag{A.6}$$

or, equivalently:

$$p(s,t) \;=\; A(s)S\big[t-\tau(s)\big]. \tag{A.7}$$

Thus, the received signal is simply a scaled and delayed replica of the source signal. The scaling factor, i.e. the change in amplitude of the source signal, is determined by the change in the cross-sectional area of a ray tube.

A key assumption in the above description is that the amplitude $A(s)$ is purely real. As discussed before, boundary reflections typically cause phase changes. In addition, Gaussian beam tracing creates more general phase changes. In short, $A(s) = A_r(s) + iA_i(s)$ is generally a complex number. We require $A(s,\omega) = A^*(s,-\omega)$, where ω is the angular frequency, to ensure the resulting waveform is purely real. In the simplest case, we can assume $A(s,\omega) = A_r(s) + i\text{sgn}(\omega)A_i(s)$, with the frequency dependence entirely embedded in the sign function. Substituting this in equation (A.3) we obtain:

$$\begin{aligned} p(s,t) \;&= A_r(s)\frac{1}{2\pi}\int_{-\infty}^{+\infty} S(\omega)e^{-i\omega[t-\tau(s)]}\,\mathrm{d}\omega + \\ &\quad A_i(s)\frac{1}{2\pi}\int_{-\infty}^{+\infty} i\text{sgn}(\omega)S(\omega)e^{-i\omega[t-\tau(s)]}\,\mathrm{d}\omega. \end{aligned} \tag{A.8}$$

Recall that the Hilbert transform $\hat{S}(t)$ is a 90° phase change of an arbitrary waveform $S(t)$, and is therefore defined by [27]:

$$\hat{S}(t) \;=\; \frac{1}{2\pi}\int_{-\infty}^{+\infty} -i\text{sgn}(\omega)S(\omega)\,\mathrm{d}\omega. \tag{A.9}$$

Since $1/(\pi t)$ is the inverse transform of $-i\text{sgn}(\omega)$, we may also write the Hilbert transform as the time domain convolution of the source waveform with (πt):

$$\hat{S}(t) \;=\; \frac{1}{\pi}\int_{-\infty}^{+\infty} \frac{S(t)}{t-\tau}\,\mathrm{d}t. \tag{A.10}$$

The frequency-domain representation is usually more convenient. In either case:

$$p(s,t) \;=\; A_r(s)S\big[t-\tau(s)\big] - A_i(s)\hat{S}\big[t-\tau(s)\big]. \tag{A.11}$$

Equation (A.11) is the complete expression for the received signal and it implies that the received waveform is a weighted sum of the original one and its Hilbert transform, with the weighting determined by the strengths of the real and imaginary parts of the amplitudes. Note that the Hilbert transform produces an acausal signal, reflecting another artifact of ray theory (see Section 4.1.3). This equation is the key result showing the form of a single echo or path, including phase changes due to propagation delay, boundary reflections, and caustic phase shifts.

This solution is valid for stationary problems, i.e. for environment and source-receiver configurations fixed throughout the duration of the propagation. For real sonar environments, this is not always a valid assumption, especially for the case of moving source and/or receiver. It is well known that a moving source/receiver in free space results in a frequency Doppler shift which is described by the simple relations obtained from a Galilean transformation. In a waveguide or stratified environment, source-receiver motion results in a more complicated Doppler structure because of multipath phenomena.

If the environment is time-varying, the arrival amplitudes and delays in equation (A.1) change continuously in time. Therefore, new values of $A(s)$ and $\tau(s)$ are required at each time step of the signal transmission. In theory, at each time step,

a new set of arrival amplitudes and delays could be computed with an entirely new ray trace from the source to the exact receiver location at that particular time step. However, this would be computationally expensive and mostly unnecessary since the changes (in amplitude and delay) are likely to be very small between time steps.

Several solutions are available in the literature to account for Doppler shifts; for the standard practical case of moving source/receiver configuration, the Vir-TEX algorithm is one of the simplest and most efficient (see [28, 29] for complete details), and allows the calculation of the received signal without the need of a time-dependent ray tracer.

Appendix B

Correlation Analysis

This section is based on [30]. Correlation analysis allows for the estimation of the impulse response of a linear systems when input-output cross-correlation and input auto-correlation are available. Consider a discrete LTI system with disturbance $v(t)$:

$$y(t) \;=\; \sum_{k=0}^{+\infty} h(k)u(t-k) + v(t). \tag{B.1}$$

Assume u and v have zero mean and $E\big[u(t)v(s)\big] \;=\; 0 \;\; \forall t, s$. The correlation function is given by:

$$R_{yu}(\tau) \;=\; E\big[y(t+\tau)u(t)\big] \;=\; \sum_{k=0}^{+\infty} h(k)R_{uu}(\tau-k). \tag{B.2}$$

If $u(t)$ is white noise ($R_{uu}(\tau) = 0$, $\tau \neq 0$), equation (B.2) is simplified to:

$$R_{yu}(k) \;=\; h(k)R_{uu}(0). \tag{B.3}$$

Cross-correlation and auto-correlation functions can be estimated from input and output signals using a finite number of samples N:

$$\begin{aligned} \hat{R}_{yu}(\tau) \;&=\; \frac{1}{N}\sum_{t=1}^{N-\tau} y(t+\tau)u(t) \quad \tau = 0, 1, 2, \ldots \\ \hat{R}_{uu}(\tau) \;&=\; \frac{1}{N}\sum_{t=1}^{N-\tau} u(t+\tau)u(t) \quad \tau = 0, 1, 2, \ldots \end{aligned} \tag{B.4}$$

Using equations (B.4), equation (B.3) can be solved to find the impulse response estimate $\hat{h}(k)$.

When $u(t)$ is not exactly white, there are two solutions:

- Apply a so called *whitening filter*: filter both inputs and outputs in order to make the input as white as possible;
- Truncate the impulse response at a certain order.

The second solution assumes that:

$$h(k) \;=\; 0 \quad k > M. \tag{B.5}$$

This is a *finite impulse response* (FIR) *filter*, or *truncated weighting function*, and M is the order of the filter.

The correlation equation becomes therefore:

$$\hat{R}_{yu}(\tau) \;=\; \sum_{k=0}^{M} \hat{h}(k)\hat{R}_{uu}(\tau - k). \tag{B.6}$$

Writing out this equation for $\tau = 0, 1, \ldots, M$ gives the linear system:

$$\begin{bmatrix} \hat{R}_{yu}(0) \\ \hat{R}_{yu}(1) \\ \vdots \\ \hat{R}_{yu}(M) \end{bmatrix} = \begin{bmatrix} \hat{R}_u(0) & \hat{R}_u(1) & \ldots & \hat{R}_u(M) \\ \hat{R}_u(-1) & \hat{R}_u(0) & \ldots & \hat{R}_u(M-1) \\ \vdots & \vdots & \ddots & \vdots \\ \hat{R}_u(-M) & \hat{R}_u(-M+1) & \ldots & \hat{R}_u(0) \end{bmatrix} \begin{bmatrix} \hat{h}(0) \\ \hat{h}(1) \\ \vdots \\ \hat{h}(M) \end{bmatrix} \tag{B.7}$$

which can be solved to obtain $\hat{h}(k)$. The system matrix is the *convolution matrix* (or *Toeplitz matrix*) of the discrete system, and it is symmetric due to the symmetry of the auto-correlation function for real signals.

Appendix C

Deconvolution via Least Squares

The *deconvolution* problem is the process of extracting the input signal in a linear system when the output signal is available (and preferably the impulse response too). Several solutions can be found in the literature; for our purposes, a deconvolution that makes use of *Tikhonov regularization* (also known as *ridge regression*) was chosen.

Deconvolution can always be written as a standard linear system of equations:

$$\boldsymbol{y} \;=\; H\boldsymbol{u}, \tag{C.1}$$

where H is the deconvolution matrix. The standard approach for its solution (known as *ordinary least squares*, or simply *least squares*) seeks to minimize the sum of squared residuals:

$$\hat{\boldsymbol{u}} \;=\; \min_{\boldsymbol{u}} \; \|\boldsymbol{y} - H\boldsymbol{u}\|^2, \tag{C.2}$$

where $\|\cdot\|$ is the *Euclidean norm*. Since matrix H could be near to singularity, and the solution therefore too sensible to numerical approximations, a regularization term can be included in this minimization. That is:

$$\hat{\boldsymbol{u}} \;=\; \min_{\boldsymbol{u}} \; \|\boldsymbol{y} - H\boldsymbol{u}\|^2 + \|\Gamma\boldsymbol{u}\|^2, \tag{C.3}$$

for some suitably chosen *Tikhonov matrix* Γ. A closed form solution is available as:

$$\hat{\boldsymbol{u}} \;=\; \left(H^T H + \Gamma^T\Gamma\right)^{-1} H^T\boldsymbol{y}. \tag{C.4}$$

The effects of regularization may be varied via the scale of matrix Γ. For $\Gamma = 0$ this reduces to the classical, unregularized, least squares solution provided that $\left(H^T H\right)^{-1}$ exists. In many cases, Tikhonov matrix is chosen as a multiple of the identity matrix $\Gamma = \lambda I$, giving preference to solution with smaller norms.

Appendix D

AcTUP Quick Start Guide

This section is based on [25]. A brief guide for setting up a simulation with the BELLHOP version included in the front-end will be given. With this toolbox, instead of writing and editing each time the .env file (Section 4.2.1) which defines the simulation, the user can exploit the simple GUI-structure of the software which provide intelligent guesses and selection guidelines for code-specific parameters.

At the end of installation instructions, after running AcTUP the user will see a menu-driven system; the following basic steps must be followed in order to configure and launch the simulation:

- *Configure Environment & Propagation Models*

  The most important section. Launches another menu which allows the user to define all the necessary environmental and simulation parameters. *Edit Environment* launches an interface to edit the model environment. The user can specify each layer's structure (water column, sediment, vacuum) and geophysical parameters. Sound speed profiles can be imported from a .txt file arranged in depth-value pairs. *Edit Code-Independent Propagation Parameters* is the section that contains the basic parameters (frequency, source and receiver depths,...) defining the propagation scenario. These parameters are common to each propagation code. *Edit Code-Dependent Propagation Parameters* is the section where additional information must be provided for some codes, reflecting their numerical features. In the case of BELLHOP, these are the simulation type (ray tracing, transmission loss, arrivals), the beam type (geometric, gaussian), the beam number, and other minor ones. All the specified settings can be saved as a .mat file with the command *Save Run Definition* for future use.

- *Select Active Code*

  Since AcTUP is a GUI-wrapper for each model included in the Acoustic Toolbox, the user can the select them with this command. The name of the current code always appears on the right.

- *Run Current Model for ACTIVE Propagation Code*

  Runs the environment/propagation model currently in memory using the selected propagation code. The simulation time is displayed in the Matlab workspace.

- *Plotting Tools*

  Simulations results (rays, transmission loss fields and slices, amplitude-delay arrivals,...) can be displayed using the commands available in this section, which are largely self-explanatory.

We must remember that BELLHOP is essentially a high-frequency code, and although its useful frequency range extends lower than standard ray trace programs, it should be used with extreme caution in situations where the water depth or the size of any significant feature in the sound speed profile is less than 20 wavelengths (see Section 4.1). In these cases, the use of another model (KRAKEN, SCOOTER) should be preferred.

Bibliography

[1] L. Paull et al. "AUV navigation and localization: A review". In: *Oceanic Engineering, IEEE Journal of* 39.1 (2014), pp. 131–149.

[2] L. Stutters et al. "Navigation technologies for autonomous underwater vehicles". In: *Systems, Man, and Cybernetics, Part C: Applications and Reviews, IEEE Transactions on* 38.4 (2008), pp. 581–589.

[3] J. C. Kinsey, R. M. Eustice, and L. L. Whitcomb. "A survey of underwater vehicle navigation: Recent advances and new challenges". In: *IFAC Conference of Manoeuvering and Control of Marine Craft*. 2006.

[4] *Woods Hole Oceanograpic Institution*. URL: `http://www.whoi.edu/`.

[5] *Teledyne Technologies*. URL: `http://www.teledyne.com/`.

[6] *EvoLogics*. URL: `http://www.evologics.de/`.

[7] B. Allotta et al. "Typhoon at CommsNet 2013: experimental experience on AUV navigation and localization". In: *Advances in Robotics and Control, IFAC* (2015, in press).

[8] A. Caiti et al. "Thesaurus: AUV teams for archaeological search. Field results on acoustic communication and localization with the Typhoon". In: *Control and Automation (MED), 2014 22nd Mediterranean Conference of*. IEEE. 2014, pp. 857–863.

[9] B. Allotta et al. "Typhoon at CommsNet 2013: experimental experience on AUV navigation and localization". In: *Proc. IFAC World Congress*. 2014.

[10] A. Caiti et al. "Experimental results with a mixed USBL/LBL system for AUV navigation". In: *Underwater Communications and Networking (UComms), 2014*. IEEE. 2014, pp. 1–4.

[11] A. Caiti et al. "Fusing acoustic ranges and inertial measurements in AUV navigation: The Typhoon AUV at CommsNet13 sea trial". In: *OCEANS 2014-TAIPEI*. IEEE. 2014, pp. 1–5.

[12] F. Di Corato et al. "Toward underwater acoustic-based simultaneous localization and mapping. Experimental results with the Typhoon AUV at CommsNet13 sea trial". In: *Oceans-St. John's, 2014*. IEEE. 2014, pp. 1–7.

[13] D. R. Topham and R. G. Perkin. "CTD sensor characteristics and their matching for salinity calculations". In: *Oceanic Engineering, IEEE Journal of* 13.3 (1988), pp. 107–117.

[14] F. B. Jensen et al. *Computational Ocean Acoustics*. Springer, 2011.

[15] J. M. Hovem. *Marine Acoustics: The Physics of Sound in Underwater Environments*. Peninsula Publishing, 2012.

[16] L. M. Brekhovskikh and Y. P. Lysanov. *Fundamentals of Ocean Acoustics*. Springer, 2003.

[17] R. J. Urick. *Principles of Underwater Sound*. McGraw-Hill, 1983.

[18] E. Lewis. "The practical salinity scale 1978 and its antecedents". In: *Oceanic Engineering, IEEE Journal of* 5.1 (1980), pp. 3–8.

[19] V. A. Del Grosso. "New equation for the speed of sound in natural waters (with comparisons to other equations)". In: *The Journal of the Acoustical Society of America* 56.4 (1974), pp. 1084–1091.

[20] F. E. Hale. "Long-range sound propagation in the deep ocean". In: *The Journal of the Acoustical Society of America* 33.4 (1961), pp. 456–464.

[21] M. B. Porter. *The BELLHOP Manual and User's Guide: Preliminary Draft*. Heat, Light, and Sound Research, Inc., La Jolla, CA, USA, Tech. Rep. 2011.

[22] A. J. Duncan and A. L. Maggi. "A consistent, user friendly interface for running a variety of underwater acoustic propagation codes". In: *Proceedings of ACOUSTICS*. 2006, pp. 471–477.

[23] *Ocean Acoustics Library*. URL: `http://oalib.hlsresearch.com/`.

[24] O. Rodriguez. *General description of the BELLHOP ray tracing program*. Universidade do Algarve. 2008.

[25] A. J. Duncan and A. L. Maggi. *AcTUP v2.2L Acoustic Toolbox User-Interface & Post-Processor–Installation & User Guide*. Curtin University of Technology, Perth. 2006.

[26] M. Stojanovic and J. Preisig. "Underwater acoustic communication channels: Propagation models and statistical characterization". In: *Communications Magazine, IEEE* 47.1 (2009), pp. 84–89.

[27] N. E. Huang and S. S. Shen. *Hilbert-Huang transform and its applications*. Vol. 5. World Scientific, 2005.

[28] M. Siderius and M. B. Porter. "Modeling broadband ocean acoustic transmissions with time-varying sea surfaces". In: *The Journal of the Acoustical Society of America* 124.1 (2008), pp. 137–150.

[29] J. C. Peterson and M. B. Porter. "Ray/beam tracing for modeling the effects of ocean and platform dynamics". In: *Oceanic Engineering, IEEE Journal of* 38.4 (2013), pp. 655–665.

[30] L. Ljung. *System Identification: Theory for the User*. Prentice Hall, 1999.